NUMERICAL STUDY OF HIGH-FREQUENCY FLUIDIC VALVE INJECTORS FOR DETONATION ENGINE APPLICATIONS

by

SUSHMA YALAVARTHI

Presented to the Faculty of the Graduate School of
The University of Texas at Arlington in Partial Fulfillment
of the Requirements
for the Degree of

DOCTOR OF PHILOSOPHY

THE UNIVERSITY OF TEXAS AT ARLINGTON

December 2019

To all my teachers.

ACKNOWLEDGEMENTS

I would like to thank my supervising professor, Dr. Frank Lu, for giving me an opportunity to work with him. His support and encouragement have been invaluable during the course of my doctoral studies. Our extended discussions helped me change my perspective towards research methodologies. I would like to thank my committee members, Dr. Donald Wilson, Dr. Zhen Xue Han, Dr. Hyejin Moon, and Dr. Habib Ahmari, for being considerate and accommodating.

I would also like to thank my fellow researches at the ARC, Dr. Sarah Hussein, Nanda Kumar, Umang Dighe, and Rohit Pulimidi, for their valuable assistance in academic and research matters. I am much obliged to Dr. Dibesh Joshi and Dr. James Peace for their experimental contributions which helped me immensely in my research work. Additionally, I am thankful to Dr. Andrew Mizener for his extended support with measurement lab course work. I would like to extend my gratitude to my dearest friend, Bhavana Sajja, who encouraged, supported, and cheered me up throughout my research in the most positive way.

I would like to acknowledge the Texas Advanced Computing Center (TACC) for providing access to their high performance computing resources.

I am indebted to my parents, Lakshmi Kumari and Venkata Rao Yalavarthi for their continuous love and support. Thanks to my brother, Rakesh Yalavarthi, for being instrumental in keeping my morale high. I am humbled and grateful to my in-laws, Ramesh Kawle and Seema Kawle, for their sense of support. I greatly cherish the people who supported me financially during my initial days in the United States.

Some special words of gratitude go to my friends, Maheswari Konidena, Vineetha Edupuganti, Vamsi Kiran Eruvaram for their constant encouragement.

Finally, I would like to thank my best friend, love of my life, my dearest husband, Ninad Kawle, for giving me extra strength and motivation throughout my endeavor.

November 21, 2019

ABSTRACT

NUMERICAL STUDY OF HIGH-FREQUENCY FLUIDIC VALVE INJECTORS FOR DETONATION ENGINE APPLICATIONS

Sushma Yalavarthi, Ph.D.

The University of Texas at Arlington, 2019

Supervising Professor: Frank K. Lu, Ph.D., P.E.

The feasibility of fluidic valves for use in detonation-based engines was studied numerically. The fluidic valve acted by shutting off reactant flow through the high pressure behind detonation waves propagating past the valve opening. The valve which featured a plenum cavity was mounted to the side of a pulsed detonation engine, an arrangement that allowed the valve to be characterized under a sustained operation. A series of different cavity lengths were studied. Further, a numerical study of the high-frequency fluidic valve was conducted by using a two-dimensional reactive Euler solver. A 19–step elementary mechanism was employed for the stoichiometric oxyhydrogen combustion. Two conditions, named as blocked cavity and air injection, were studied. Insights into the complex behavior of the shock wave interactions within the fluidic valve cavity were obtained. The pressure histories of the incident shock and the subsequent reflections within the cavity were tracked via wave diagrams. The wave diagrams indicated that the longer cavities induced reflections for a longer duration in both the blocked and air-injection configurations, with the latter showing more complicated flows. The numerical trends were similar in terms

of non-dimensional pressure and interruption time, agreeing with the experimental results of Peace et al. (2014) but disagreeing with earlier single-shot results. Further simulations, by changing the position of the fluidic valve with respect to the thrust wall of the detonation tube reiterated the importance of fluidic valve location. The numerical findings include the backflow plots which represent the required refueling time with respect to the arrival of the fresh combustible mixture inside the detonation tube.

TABLE OF CONTENTS

LIST OF ILLUSTRATIONS

LIST OF TABLES

NOMENCLATURE

A_r	Pre-exponential Arrhenius factor for reaction
CJ	Chapman–Jouguet
$C_{j,r}$	Molar concentration of j^{th} species in reaction r
$c_{p,i}$	Specific heat at constant pressure of species i
c_p	Specific heat at constant pressure
E	Total energy per unit mass
E_r	Activation energy of reaction r
$\mathbf{F}$	Convective flux vector in x-direction
$\mathbf{G}$	Convective flux vector in y-direction
$k_{b,r}$	Backward rate reaction constant
$k_{f,r}$	Forward rate reaction constant
h	Specific enthalpy
h^o	Sensible enthalpy
K_r	Equilibrium constant
L_i	Distance between detonation channel head end and the orifice
$\mathcal{M}_i$	Detonation of species i
$M_{w,i}$	Molecular weight of species i
N	Number of species in the system
N_R	Number of reactions
n	Temperature exponent in Arrhenius relation
p	Pressure
p_0	Initial detonation tube pressure

p_{CJ} Chapman–Jouguet detonation pressure

p_p Steady-state plenum pressure

PDE Pulsed detonation engine

$\mathbf{Q}$ Flow variable vector or state vector

q Energy input

RDE Rotating detonation engine

R Gas constant

R_i Net rate of production of species i

T Temperature

t Time

t_b Backflow time

t_{int} Interruption time

U Detonation wave speed

u Flow speed

V_x Velocity in x-direction

V_y Velocity in y-direction

$\mathbf{W}$ Species source vector

x Axial distance into the cavity from the orifice location

Y_i Mass fraction of species i

ZND Zel'dovich–von Neumann–Döring state

ρ Density

α Shape factor

$\eta'_{j,r}$ Stoichiometric coefficients for the reactants

Π Non-dimensional pressure

Γ Net effect of third bodies on the reaction rate

γ Ratio of specific heats

τ Non-dimensional interruption time

τ_b Non-dimensional backflow time

$v'_{i,r}$ Stoichiometric coefficient of reactants

$v''_{i,r}$ Stoichiometric coefficient of products

$v''_{j,r}$ Stoichiometric coefficient of products

Subscripts

1 Initial state

2 Final state

CJ Chapman–Jouguet state property

CHAPTER 1

INTRODUCTION

Detonation-based engines can be categorized as pulse detonation engine (PDE), standing detonation engine (SDE), and rotating detonation engines (RDE). Among these, PDEs and RDEs have a wide range of operation and hence these engines are of much current interest for aerospace propulsion and power applications. The detonation process was fundamentally described by Berthelot et al. in 1881 [1]. A zero-dimensional theory of detonation was developed independently by Chapman and Jouguet [2]. This theory helped advance the research of detonation engine by Nicholls at the University of Michigan in the late 1950s [3]. Nicholls made the first attempt to demonstrate the application of pulse detonation to jet propulsion. Further, the establishment of continuously rotating detonation was demonstrated in 1960 by Voitsekhovskii et al. [2]. Following a hiatus, intensive research on PDEs and RDEs was reinitiated in 1990s. Research on detonation-based engines started at the University of Texas at Arlington (UTA) in 1994 in a program that was funded by the University of Texas Systems Advanced Technology Program [4]. In this program, UTA performed an experimental investigation of fundamental detonation physics, followed by the development of a series of small-scale PDEs.

Unlike deflagration (subsonic combustion), a detonation's (supersonic combustion) flame front propagates with a velocity of the order of km/s. This produces a significant pressure increase than deflagration [5]. Also, the pressure rise for fuel-oxygen mixtures can be 20 times higher than for conventional jet engines [1]. In contrast to detonation, deflagration flame velocities are of the order of m/s. In conventional

jet engines, the combustion chamber pressure drops slightly due to combustion [6]. Also, there is a possibility of high emission of NO_x with arrangements such as turbine cooling, and afterburner combustion [6]. The application of detonation to jet engines offers a relatively low emission of NO_x with the lean mixture detonation propagation [1]. Such engines offer a significant improvement to the engine performance where the efficiency of the engine cycle can be theoretically increased by 15% [1].

Detonation-based propulsion is being explored in recent times to achieve advances in performance of air-breathing engines and rocket engines [7]. Initial research on PDEs was conducted by Eidelman et al. in the early 90s [8], [9]. Bussing et al. developed the basic theory, and design concepts related to pulse detonation engines [10]. Kailasanath et al. presented the performance estimates and nozzles for pulse detonation combustion systems [11], [12]. Kailasanath et al. reviewed the significant progress in the development of PDEs for air-breathing and rocket engine applications during the 1990s [11]. Kailasanath et al. also mentioned the significance of the development of inlets and nozzles for PDEs [11]. Roy et al. emphasized the importance of valveless PDEs and better filling processes to achieve efficient thrust for flying vehicles and power production in-surface plants [13]. Kailasanath et al. discussed the development of PDE combustion systems and mentioned the need for research on efficient and fast injection system for practical applications [14]. The primary focus of these studies in the past decade has been on the PDE concept. Wilson et al. summarized the system integration studies for both PDE and RDE in 2011 [4]. Lu et al. published a comprehensive review on RDE experimental challenges, modeling, and engine concepts in 2014 [15]. The concepts of PDE and RDE have gained a wide range of interest. There is a potential to achieve better engine performance and new concepts are being developed worldwide.

1.1 PDE Operation

Figure 1.1 shows a generic PDE cycle. As shown in the figure, the PDE is a long tube with a closed end and an open end for the exhaust. PDE operation mainly comprises three processes, namely, filling, ignition, and blowdown. In the filling process, the PDE tube is filled with a reactive gas mixture through the filling valves. These valves will shut once the tube is filled with the reactants following which the ignition system is activated [16]. In the ignition process, the flame is ignited and transitions to a high-pressure detonation wave. This high-pressure detonation wave further propagates through the combustion chamber [13]. During the blowdown process, an expansion wave travels back into the tube as the hot combustion gases move out. Thrust is produced when the wave exits the tube [7], [13], [14], [16]. As the trailing edge of the expansion wave arrives at the closed end of the combustion chamber, fresh reactants enter the tube, thus refilling occurs and hence the cycle repeats. These fresh reactants may come in contact with residual hot gases of the previous cycle resulting in undesirable autoignition since it is uncontrollable [10]. This deflagration may even form a detonation front during the purging process [10].

Unlike ramjet engines, PDEs can be operated at static conditions. This can be done with the help of a fan at the entrance of the combustor to force air into the chamber [7]-[10]. But, in general for aerospace applications, PDEs can operate through a wide flight Mach number range of 0 to 5 with an operating frequency of the order of 100 Hz. However, with mechanical valves, the propellant flow may not be fast enough to meet the demands associated with high thrust production [13]. Also, the rapid closing of such valves may result in the formation of hammer shocks [16]. Moreover, various applications of air-breathing propulsion require a continuous mode of operation. Although rapid refilling is essential, the gas prior to detonation will likely be near-stagnation conditions. In order to achieve a continuous mode of operation,

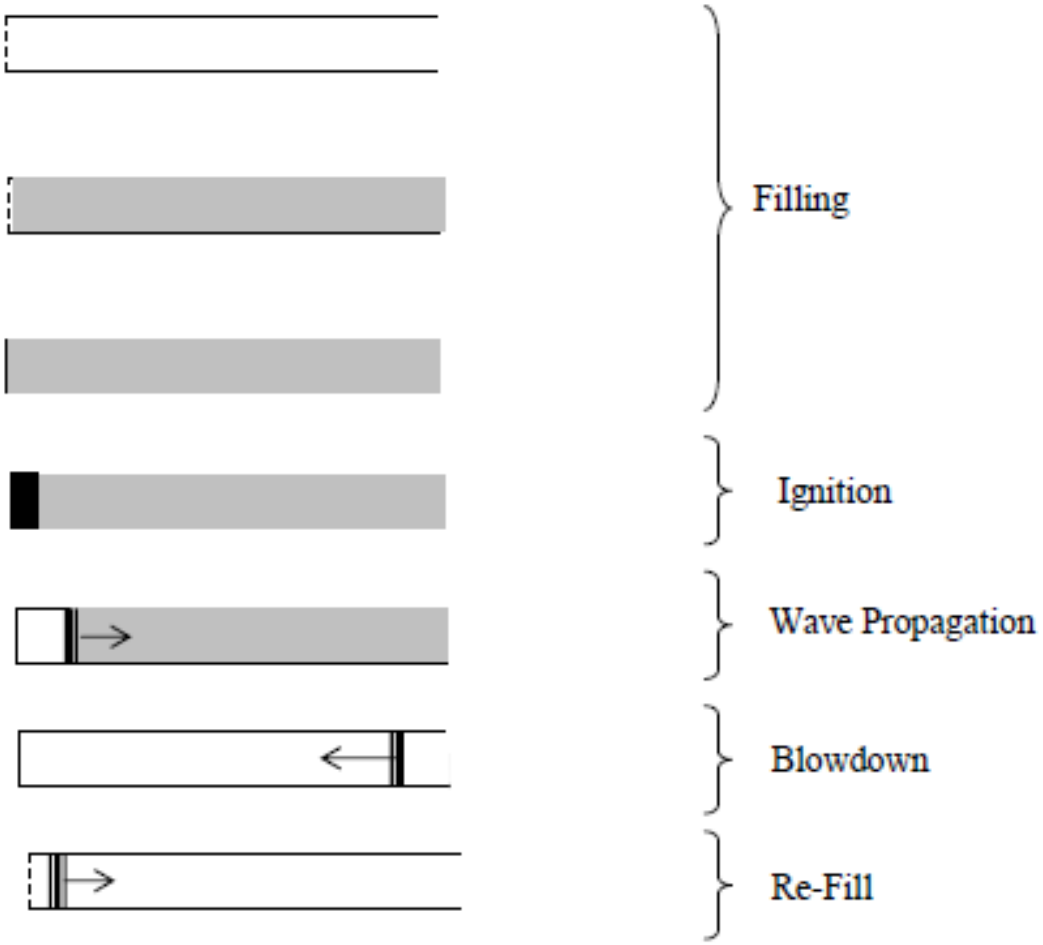

Figure 1.1: PDE operation [17]

valves with a fast response time are required. At high operating frequencies, self-regulated valveless PDE can provide such a fast shut-off time.

1.2 RDE Operation

The operating frequency of the rotating detonation engine (RDE) is of the order of 1–10 kHz [18]. In RDEs, the combustion chamber is an annulus in which a detonation wave propagates circumferentially in a continuous manner by consuming reactants [12], [15], [16]. The continuous supply of reactants is from injectors around

the annulus, normal to the direction of the detonation wave propagation [15], [16], [17], [19] [20]. The combustor pressure gain helps to temporarily block the injector flow [21]. Due to the gasdynamic interactions inside the combustor, the reduced pressure allows fresh reactants into the combustor [16], [21]. Similar to PDEs, rapid refilling is crucial for RDE operation [16], [22], [23]. Also, RDEs can operate in a wide range of flight Mach number of 0 to 5.

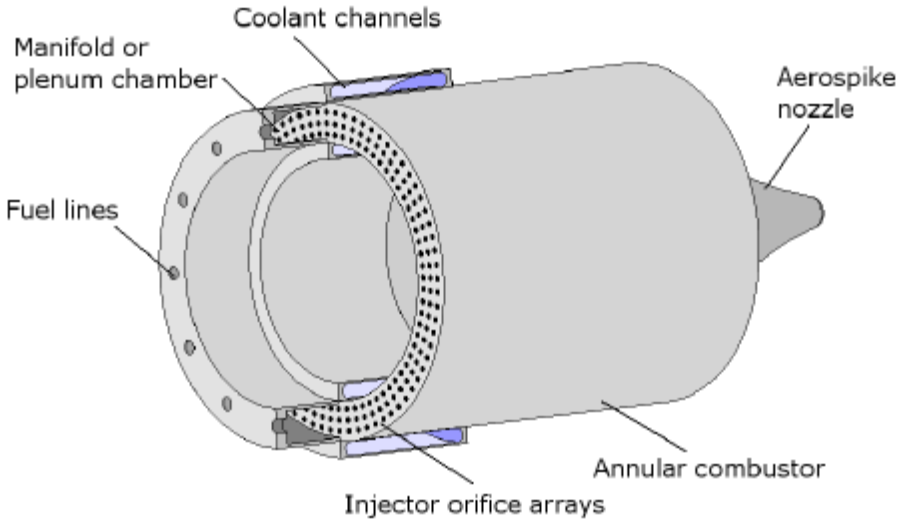

Figure 1.2: RDE schematic [16]

Figure 1.2 shows schematic of RDE configuration. An unwrapped schematic showing the wave structure of the RDE is presented in Fig. 1.3. In RDE operation, reactants are fed either separately or premixed into an annular combustor through an array of micronozzles [12]. A detonation wave propagates in the annulus by consuming the reactants feeding continuously from the bottom end of the combustion chamber [12], [16]. The gas expands axially and azimuthally.

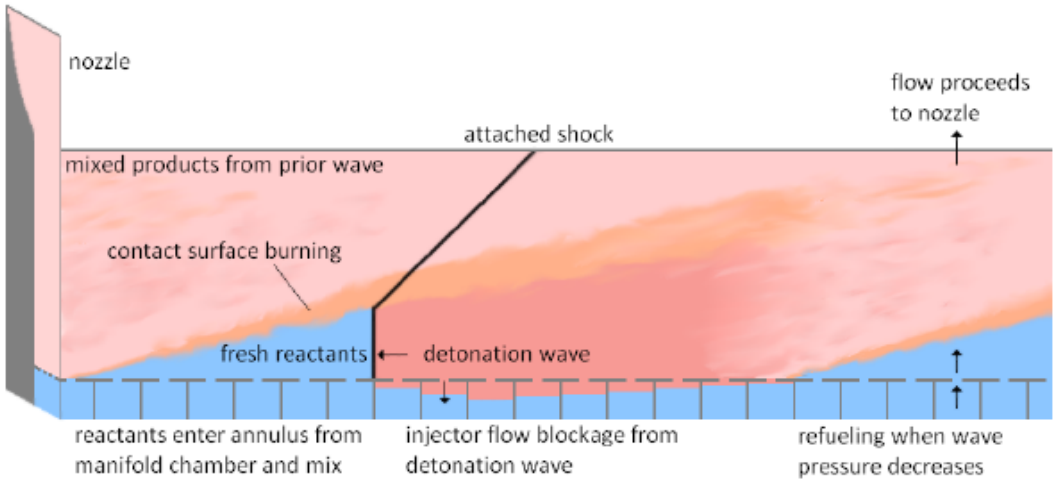

Figure 1.3: RDE wave structure [16]

Figure 1.3 shows that behind the detonation front, the reactive mixture begins to penetrate into the combustion chamber. The high pressure behind the detonation wave blocks the injector flow entering the tube. Contact surface burning is shown in Fig. 1.3 because of the possibility of the temperature of the hot gases exceeding the autoignition temperature [16], [24]. The contact surface burning separates the mixed products from the prior wave and fresh reactants. The degenerated detonation wave, also known as secondary shock wave or the blast wave separates the burned non-detonated products and fresh reactants. This wave was previously known as a combined detonation-blast wave or detonation wavelet [25], [26]. As the flow proceeds to expand, the secondary shock wave will relatively become weaker leading to refueling. Thus, the cycle repeats.

1.3 Motivation

Fuel injection with the mechanical valves for PDE has been successfully demonstrated for the cycle frequencies of about 100 Hz in a single tube [11], [13]. For RDEs

with higher operating frequencies, continuous, stable, and uninterrupted fuel flow is required. To do so, efficient fuel injection valves are required which can provide uninterrupted fuel flow. PDEs utilize single detonation wave during one operating cycle whereas, RDEs can have multiple detonation waves in a single cycle. The presence of multiple detonation waves complicates the working of RDE. Perpendicular fuel impingement may disrupt the steady-state wave propagation. On the other hand, the passing of multiple wavefronts can obstruct the incoming fuel flow. This condition is called a backflow condition and it has been shown to occur [27], [28]. Elimination of backflow conditions is essential for the working of RDE. This is because prevailing of the condition for a period more than the cycle time will result in cutting off the fuel supply. Based on the design of rocket injector manifolds, Nicholls et al. designed injectors for fuel and oxidizer [27]. The novelty in design came from the way the fuel and oxidizer can be fed separately [27]. The presence of the mixing chamber ensures the premixing of the fuel and oxidizer [27]. Similar developments in the fuel injection system were employed by Bykovskii et al. [29], [30].

An air-breathing RDE has been analytically studied by Mizener et al. [31]. Working of an RDE is similar to the working of a PDE in some aspects. Numerical simulation presumes injection valve for RDE [32], [33]. This injection valve has a series of micronozzles or orifices [32], [33]. With this arrangement, due to the high pressure of the detonation wave, the fuel valves are temporarily blocked [32], [33]. Braun et al. experimentally investigated the potential of such valves for high operational frequency PDE [34]. Such valves were named as fluidic valves by Braun et al. [34]. The fluidic valves are designed to optimize the characteristics such as overall geometry, backflow time and backpressure based on the experimental results [34]. A plenum cavity is essential for the operation of the fluidic valve. The plenum cavity restricts the backflow of the detonation products during the PDE cycle. The fluidic

valve requires a small plenum cavity placed beneath the injector orifice which helps to act against combustion products entering the valve after each revolution of the detonation wave [34]. A fluidic valve with a cavity was proposed by Braun et al. [34] that utilized the high pressure of the detonation wave entering the cavity to achieve a controlled interrupted propellant flow. In essence, the fluidic valve provided a means of high-frequency injection that was coupled with the dynamics of detonation waves within the engine. This allows for a non-electromechanical valve whereby controlled interruption times were synchronized to the operating conditions of an RDE or, more appropriately, the subsequent passing of detonation wavefronts across the injection orifices of the valve. Recent experimental and computational studies have been conducted to assess its feasibility with different fuels, combustor pressures, and injection strategies [18], [33]. Braun et al. [34] presented a parametric study on the possibilities of various types of fluidic valve orifices with constant cavity geometry. Their single-shot experiments identified key parameters in the valve opening and closing processes due to wave interactions [34]. However, an anomalous behavior was found with the argon data appearing to be inconclusive [34]. This may be due to a change in the wave behavior [35]. Peace et al. demonstrated the feasibility of the fluidic valve with a plenum cavity of various lengths which were integrated with PDE [35]. Also, the experimental trends [35] in terms of non-dimensional pressure and interruption time disagreed with earlier single-shot results [34]. This calls for further investigation using computational methods which leads to the motivation of this study.

1.4 Research Objectives

The current work is the computational study of a fluidic valve with a plenum cavity of various lengths. In the experiment, the valve was mounted to the exit of a pulsed detonation engine (PDE) operating with a frequency of 20 Hz [35]. While

the PDE was unable to duplicate the high frequencies of an RDE, it provided an environment where the valve would have been subjected to repeated pulses and would have achieved a quasi-equilibrium state [35]. Thus, any transient wave interactions as may occur in a single-shot operation that was not associated with sustained operation would have disappeared [35]. Two configurations were examined. In the first, the reactant feed was blocked so that the cavity was at approximately atmospheric conditions [35]. In the second configuration, the high-pressure air was used for safety reasons as a surrogate for reactants and entered the PDE [35]. Preliminary results of the propagation of detonation waves in the plenum cavity were presented in [35]. A numerical study of the single-shot operation of similar high-frequency fluidic valves was conducted. Due to the computational expense, smaller valves were studied numerically for both the blocked and air injection configurations. The present study provides a further analysis into the experimental and computational results, providing insight into the complex wave behavior of the shock wave interactions inside the fluidic valve cavity for RDE operations.

1.5 Background

Traditional internal combustion (IC) and compression ignition (CI) engines employ deflagration to convert chemical energy into mechanical energy [5]. On the other hand, PDEs and RDEs utilize detonation to convert chemical energy into useful thrust [5]. Detonation is the supersonic mode of combustion, wherein a detonation wave is a shock wave sustained by the energy released by combustion [5]. Understanding detonation theories and thermodynamics behind the theories is essential to comprehend the working of PDEs and RDEs. The following sections elaborate on the essence of detonation theories and detailed chemical analysis of oxyhydrogen detonation.

1.5.1 Detonation Theories

1.5.1.1 Thermodynamics

Figure 1.4 depicts a fixed control volume for a one-dimensional detonation wave. Rankine and Hugoniot were the first to develop this theory [36], [37]. Equations (1.1)-(1.3) are also known as Rankine–Hugonoit conditions [36], [37]. It is assumed that the flow is steady, one-dimensional, constant-area, adiabatic, with negligible body forces, and the gas is ideal.

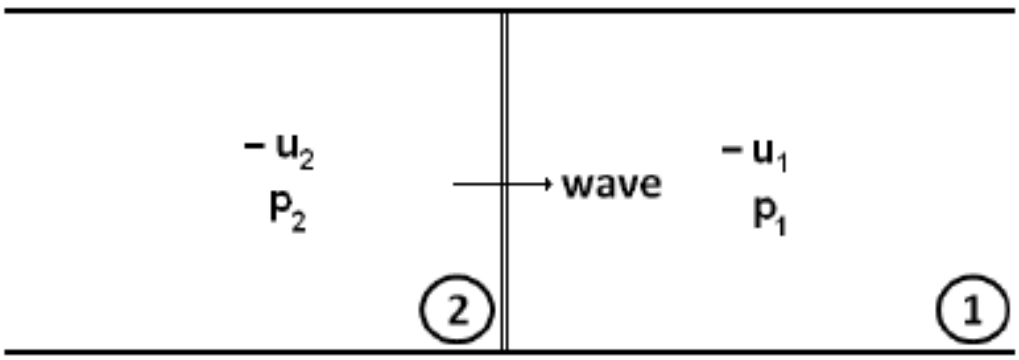

Figure 1.4: Schematic of one-dimensional control volume for detonation [16]

$$\rho_1 u_1 = \rho_2 u_2 \tag{1.1}$$

$$p_1 + \rho_1 u_1^2 = p_2 + \rho_2 u_2^2 \tag{1.2}$$

$$c_{p,1} T_1 + \frac{1}{2} u_1^2 + q = c_{p,2} T_2 + \frac{1}{2} u_2^2 \tag{1.3}$$

Here, q is the heat added due to the chemical energy release. For a shock wave, this term is zero.

$$p_1 = \rho_1 R_1 T_1 \tag{1.4}$$

$$p_2 = \rho_2 R_2 T_2 \tag{1.5}$$

If c_p is constant, equations (1.1)-(1.3) have unknown parameters viz. T_2, p_2, ρ_2, u_1, and u_2. Chapman and Jouguet further developed the one-dimensional detonation wave theory for an infinitesimally thin detonation [38], [39]. Their combined work is popularly known as the Chapman–Jouguet theory (CJ theory). The CJ theory was further developed independently by Zel'dovich, von Neumann, and Döring [40], [41], [42]. Their combined work is widely known as Zel'dovich–von Neumann–Döring (ZND) model. The ZND model also utilizes the one-dimensional detonation wave theory for an infinitesimally thin detonation to provide insight into the high-pressure point also known as the von Neumann spike.

The total enthalpy in a mixture and the heat addition can be written as

$$h = c_p T + h^o \tag{1.6}$$

$$q = h_1^o + h_2^o \tag{1.7}$$

Further modifying equations (1.1) and (1.2) provides equation (1.8) in terms of u_1 and u_2

$$u_1^2 - u_2^2 = \Big(\frac{1}{\rho_1} + \frac{1}{\rho_2}\Big)\Big(p_2 - p_1\Big) \tag{1.8}$$

Combining the equations (1.3) and (1.8) gives

$$c_{p,2}T_2 - c_{p,1}T_1 = q + \frac{1}{2}\Big(\frac{1}{\rho_1} + \frac{1}{\rho_2}\Big)\Big(p_2 - p_1\Big) \tag{1.9}$$

Equation (1.9) can be rewritten by including the specific heats to yield the Rankine-Hugoniot equation

$$q = \frac{\gamma}{\gamma - 1}\Big(\frac{p_2}{\rho_2} - \frac{p_1}{\rho_1}\Big) - \frac{1}{2}\Big(p_2 - p_1\Big)\Big(\frac{1}{\rho_1} + \frac{1}{\rho_2}\Big) \tag{1.10}$$

Figure 1.5 shows Rankine-Hugoniot curves created for real gas combustion of a stoichiometric H_2–air mixture [16] where α is the shape factor and can be defined as

$$\tan\alpha = \frac{p_2 - p_1}{(1/\rho_1) - (1/\rho_2)} \tag{1.11}$$

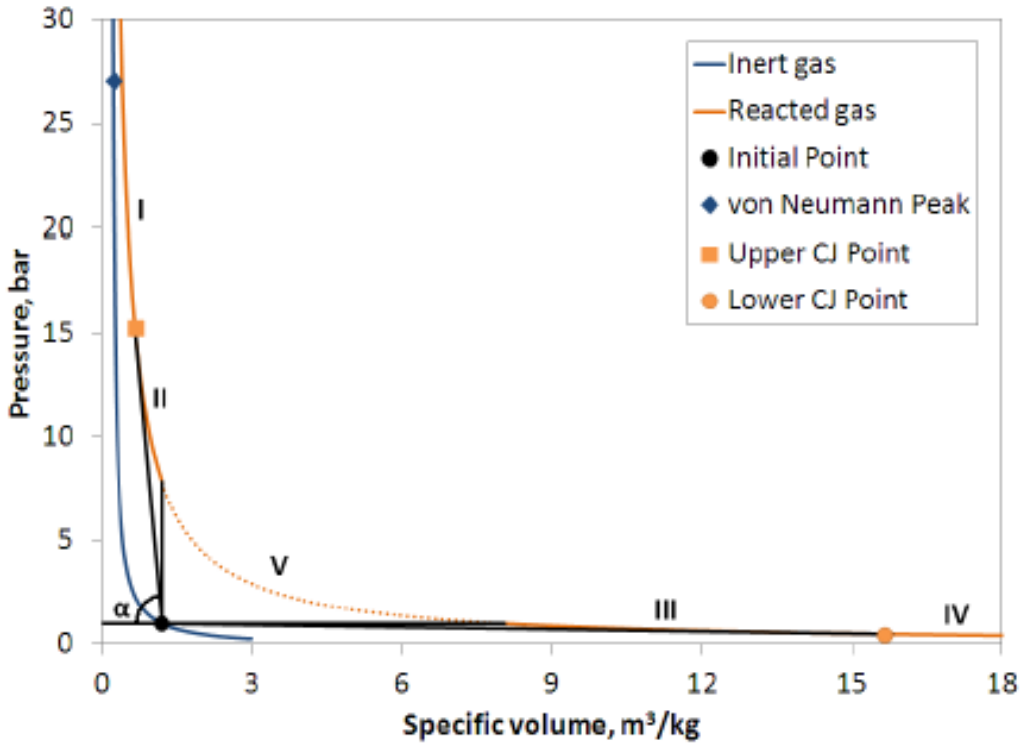

Figure 1.5: Hugoniot curves for stoichiometric H_2–air combustion [16]

These curves were created using the equations (1.8) and (1.10) where the flow was assumed to be adiabatic. The Rankine-Hugoniot curve depicts shock and expansion waves at varying conditions. The upper and lower CJ points represent compression and expansion wave at high speed and low speed respectively. For Figure 1.5, the compression and expansion wave speeds are 1968 and 51 m/s respectively [16].

The Rankine-Hugoniot curve is divided into five regions. Detonation is represented by regions I and II where the condition for strong detonation is associated with region I and the condition for weak detonation is attributed to region II. In terms of gas velocities, regions I and II exhibit different behavior. Gas velocities are

supersonic before the wave and subsonic after the wave for region I. On the other hand, gas velocities are supersonic before and after the wave in region II. In region I, the velocity of the burned gases behind the detonation wavefront is subsonic. The formation of rarefaction wave makes region I unstable. This instability will continue until the wavefront reaches the upper CJ point. At the upper CJ point, the conditions behind the wavefront become sonic. Conversely, burned gases in region II overtake the wavefront obstructing the flow propagation. This results in instability in region II. In region I, the von Neumann peak was plotted corresponds to the high-pressure condition before heat addition. Deflagrations are represented by regions III and IV. Region III encompasses lower CJ point and represents the laminar flow of the wavefront where gas velocities remain subsonic. Region IV starts after lower CJ point and can be deemed physically impossible. This is because the gas velocity spikes to the supersonic region after the subsonic wave. In region V, the Rankine–Hugonoit relations are not satisfied because it violates the second law of thermodynamics and hence the region has been plotted as a dashed line [16].

Figure 1.6 shows the Rankine-Hugoniot curves with non-ideal ZND structure paths. These curves were drawn to depict the traversing of the von Neumann point at non-equilibrium conditions.

The tangential line that joins upper CJ point to the von Neumann point portrays Rayleigh heat addition at local thermodynamic equilibrium. Path ‘a’ and ‘b’ depicts deflagration and heat release processes, wherein path ‘a’ illustrates the path of shock waves that reach the von Neumann point. Path ‘c’ conditions are physically impossible since shock waves cannot reach CJ point instantly after combustion [16].

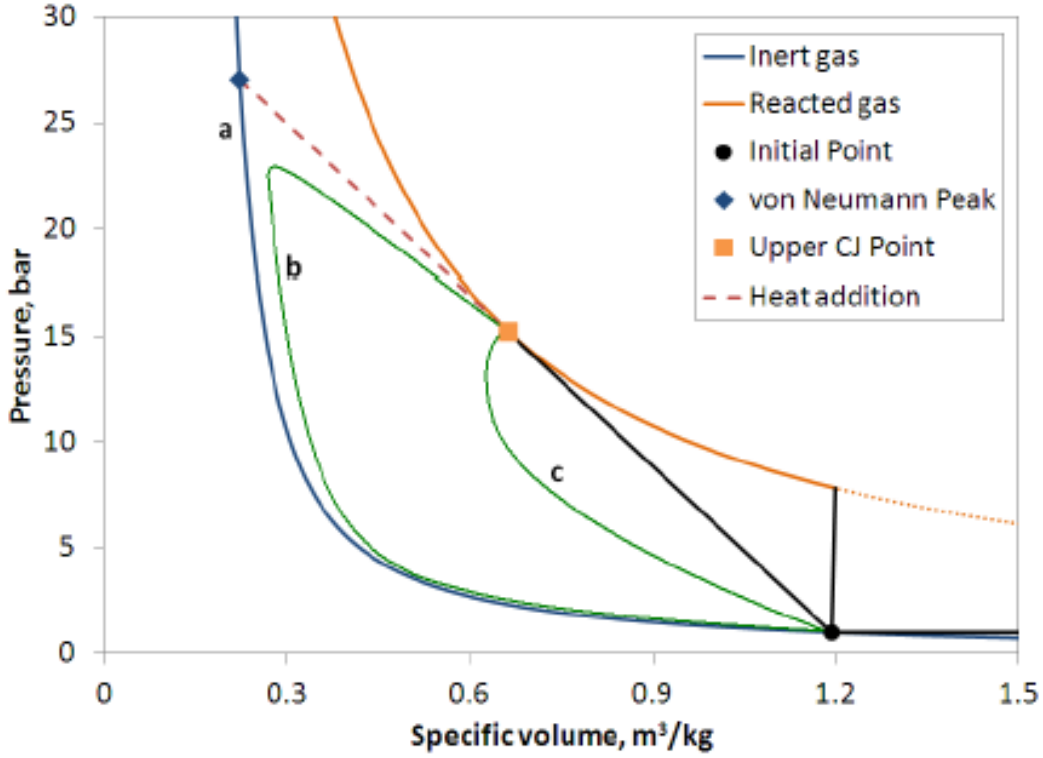

Figure 1.6: Hugoniot curves with non-ideal ZND structure paths [16]

1.5.1.2 Three-Dimensional Structure

In section 1.5.1.1, the basic detonation theories required to understand detonation wave propagation and the factors affecting were discussed. Although a one-dimensional detonation wave was presumed during the discussion, detonation waves possess a three-dimensional structure. The current section provides an insight into the complexities associated with such a structure. As illustrated in Fig. 1.7, the three-dimensional wavefront comprises of incident shocks, transverse waves, Mach stems, and slip lines [43]. The structure depicts detonation wavefront behind the leading shock. The length of the induction zone determines the geometry of the detonation cell.

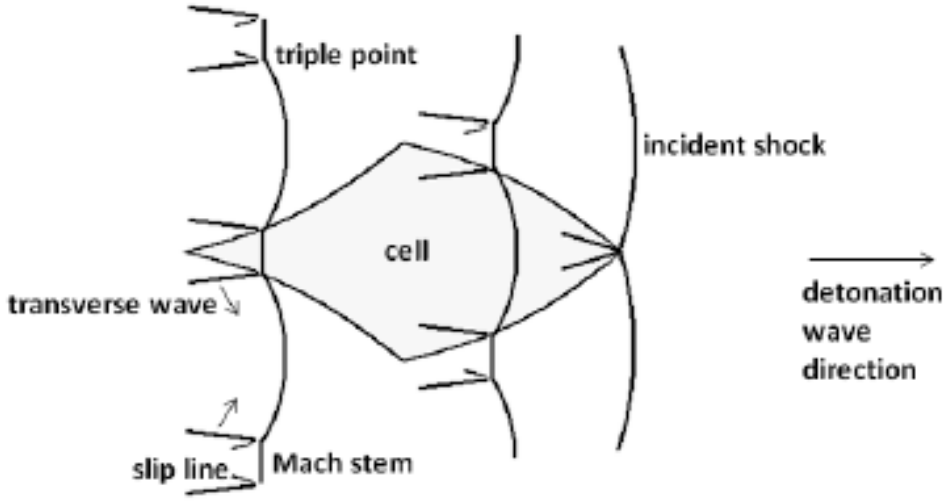

Figure 1.7: Three-dimensional detonation wave structure [43]

In Fig. 1.7, the right end represents the combustible mixture and the left end represents the reaction zone immediately behind the shock front. The curved lines are the incident shocks that instigate detonation. Mach stems results from the amalgamation of the incident wave and the reflected blast waves. These waves typically generate a pressure higher than the incident wave. Transverse waves are the reflected shock waves. The intersection of the incident shock, transverse wave, and the Mach stem is known as the triple point. Slip lines separate Mach lines from incident shocks. On the other hand, the movement of transverse waves away from the Mach stems weakens the Mach stems. Schlieren imaging and planar laser-induced fluorescence have been utilized to demonstrate the detonation wavefront and the reaction zone behind the detonation wavefront. Also, the detonation cell size depends on the composition and state of the reactive mixture [44].

1.5.1.3 Hydrogen–Oxygen Detonation Chemistry

Ma et al. illustrated the shortcomings of single-step chemical reactions in PDEs [45]. Multi-step and single-step chemical reactions for methane-air, hydrogen-oxygen and hydrogen-air hydrogen were explored inside the PDE by Li et al. and He et al. respectively [46], [47]. He et al. concluded that detailed chemical kinetics were competent enough to qualitatively capture the PDE performance [47]. Westbrook et al. , and Yetter et al. studied the combustion of hydrogen-oxygen mixtures [48], [49]. Based on their analysis, it can be concluded that the combustion process of hydrogen-oxygen mixtures mainly consists of initiation, branching, and termination processes.

For hydrogen-oxygen detonations, the intermediate H_2O and the molecule H_2 serve as third bodies. In the initiation process, due to the high energy supply, the individual molecules of H_2 and O_2 form the free radicals O, H and OH. The following equations are some examples of the initiation process.

$$H_2 \rightleftharpoons H + H \tag{1.12}$$

$$O_2 \rightleftharpoons O + O \tag{1.13}$$

Branching is also known as propagation, wherein free radicals are formed. The formation of O, H and OH fall under strong branching, whereas reactions that result in intermediates such as HO_2 and H_2O_2 are considered weak branching reactions. The following reactions show some of the branching steps. Third-body collisions (M) is formed due to a further increase in the pressure. These three-body collisions facilitate the beginning of the termination process:

$$H + O_2 \rightleftharpoons O + OH \tag{1.14}$$

$$O + H_2 \rightleftharpoons H + OH \tag{1.15}$$

$$OH + H_2 \rightleftharpoons H_2O + H \tag{1.16}$$

$$HO_2 + H_2 \rightleftharpoons H_2O_2 + H \tag{1.17}$$

Highly exothermic formation of intermediates such as HO_2 and H_2O_2 are recombined as molecules which are less reactive than the free radicals characterized termination process. Some of the terminating reactions are as follows:

$$H + O_2 + M \rightleftharpoons HO_2 + M \tag{1.18}$$

$$O + O + M \rightleftharpoons O_2 + M \tag{1.19}$$

$$H + O + M \rightleftharpoons OH + M \tag{1.20}$$

$$H + OH + M \rightleftharpoons H_2O + M \tag{1.21}$$

1.5.2 Literature Review

Fickett et al. [50] numerically investigated the idealized time-dependent, one-dimensional, piston-supported detonation using the method of characteristics. For this investigation, Fickett et al. assumed that the fluid is an ideal gas that obeys the Arrhenius gas law. This investigation converged with the linearized stability analysis of the steady detonation of Erpenbeck [51] and also found that the pressure of the shock wave almost reaches the steady-state solution with 50% higher peak pressure. Abousief et al. analytically and numerically examined the one-dimensional, piston-supported detonation for a one-step, first-order, irreversible reaction that obeys the Arrhenius gas law [52]. This study demonstrated shock perturbations and temperature fluctuations of the induction zone [52]. He et al. also studied the dynamic limit of one-dimensional detonations using linear stability analysis and direct numerical

simulation (DNS) [53]. Their studies found that the detonation propagation will be stable when the activation energy is smaller than a critical value [53].

Yu et al. [54] analyzed the detailed derivation of fundamental equations for chemically reactive flows from first principles. Their study solved the governing equations of different forms such as the conservative, non-conservative, and characteristic forms. This study could not justify the Damköhler number as unity when using multiple chemical reactions. However, their study indicated that numerically stable solutions can be found with special treatment to the species stiff term. Sekar et al. [55] numerically investigated the characteristics of PDE by using one-dimensional, two-dimensional axisymmetric models with different fuels such as H_2–O_2 and C_3H_8–air. It was concluded that careful treatment of finite-rate chemistry is required to obtain the von Neumann spike. This study indicated that closed-end initiation produces stable detonations than open-end initiation. For the axisymmetric model, with the aft-end initiation, the transmitted wave reversed its direction and may lead to engine unstart problems. This study also addressed the importance of constant-pressure boundary conditions in PDE computational domains.

Bussing et al. [56] demonstrated the PDE concept by conducting one-dimensional numerical studies using 18–step mechanisms of hydrogen-air and hydrogen-oxygen mixtures. Their results indicated that the detonation velocity is higher for a hydrogen-oxygen mixture (2850 m/s) than for a hydrogen-air mixture (1950 m/s). An analytical comparison of the constant volume, detonation cycle with constant pressure, combustion cycle was made by Bussing et al. This comparison concluded that the constant volume, detonation cycle yielded 50% higher thermal efficiency than the constant pressure, combustion cycle. Clutter et al. [57] performed a comprehensive comparison of different complex mechanisms for the appropriate treatment of the scales associated with the chemical kinetics. Some of these mechanisms include the 32–step

model of Jachimowski [58], the 7–step model of Shang et al. [59] and the 8–step model of Moretti [60] were studied. These studies concluded that the 7–step model results aligned with the scaling factor scheme and with experiments.

Hsu et al. [61] carried a numerical study of detonation in a premixed hydrogen-air mixture to investigate detonation wave propagation, to obtain ZND structure and to study the effects of chemical kinetics. For their study, Hsu et al. used the 1, 2, 7 and 38–step models proposed by Varma et al. [62], Rogers et al. [63], Shang et al. [59] and Vajda et al. [64] respectively. Hsu et al. performed a zero–dimension analysis to show chemical induction times. Results indicated that the 7 and 38–step models show a longer induction time while no significant induction time was shown for the 1 and 2–step models. Except for the 7–step model, lean mixture detonation results matched with Kistiakowsky et al.'s experimental results [65].

Sharpe et al. [66] performed one-dimensional numerical simulations of idealized detonations using a second-order Godunov scheme with different activation temperatures. In this study, Sharpe et al. found consistent results with lower activation temperatures, whereas the results with higher activation temperatures disagreed with the previous studies of He et al. [53] due to inadequacy in their numerical resolution. Also, for larger activation temperatures, the decay and reignition followed similar trends with the phenomenon observed in square tubes by Fickett et al. [50]. This analysis further emphasized that one-dimensional numerical simulations require higher activation energies and a fully-resolved induction zone.

Kailasanath et al. [67] discussed and reviewed computational studies of PDEs. Kailasanath et al. focused on the factors affecting PDE performance such as geometry, grid resolution, outflow boundary conditions and initial conditions for detonation initiation. It was concluded that close-end initiation provided a rapid initiation and establishment of the detonation wave. On the other hand, open-end initiation em-

phasized the possibility of valveless PDE operation. Kailasanath et al. observed that among different initiation techniques such as direct initiation, deflagration-detonation-transition (DDT), shock-detonation-transition (SDT) and transition from a predetonator, direct detonation is best suited for numerical simulations. Kailasanath et al. concluded that a constant pressure boundary condition or a fixed outflow boundary condition best fits PDE problems and does not affect the inside flow of the computational domain. Kailasanath et al. stated that a PDE attached to a converging-diverging nozzle produced a small portion of negative thrust due to over expansion in the diverging section of the nozzle.

Kailasanath [7] presented the developments in detonation propulsion. It was found that the detonation cycle efficiency is nearly about the constant-volume cycle efficiency. Kailasanath provided insight into stabilized normal detonations, intermittent detonations, rotating detonations, oblique shock-induced detonations, laser-supported detonations (LSDs) and oblique detonation waves (ODWs). For stabilized normal detonations, cold hydrogen gas was injected at the throat of a converging-diverging nozzle but no combustion occurred due to the insufficient residence time. For a hydrogen-air mixture, intermittent detonations were attained with a specific impulse of 2100 s. Oblique shock-induced detonations were induced by wedges that generate oblique shock followed by a normal shock wave. This theory further developed as oblique detonation wave engines (ODWEs) which showed analytically better performance than the equivalent scramjet engines for higher Mach numbers such as 15 and above. Laser-supported detonations (LSDs) uses a laser to produce detonations. This idea fetched the possibility of highly controllable exhaust velocity.

Hwang et al. [68] examined the one-dimensional pulsating overdriven detonation flowfield by utilizing an essential non-oscillatory scheme (ENO scheme) with single-step reaction kinetics. In this study, the effects of grid size on the detonation

wave, reaction zone resolution for hydrogen-air detonations were studied. This study concluded that the grid size has a significant effect on computational expense and reaction zone of at least 20 points per reaction zone length is required for accurate resolution of the detonation wave. Law et al. [69] reported the development of reaction mechanism and the role of detailed chemical kinetics in combustion phenomenon. The chemical kinetic mechanism of H_2–O_2 mixture was explained in this study and it also emphasized the role of the transport coefficients in the combustion modeling. Law et al. proposed the reduced mechanism of chemical kinetics without losing the comprehensiveness of detailed kinetics in–order–to reduce the computational expense. This mechanism results were matched with the experiments as well.

Yungster et al. [70] numerically investigated one-dimensional detonations by utilizing a detailed finite rate chemistry model for the hydrogen-air mixture. For this study, Yungster et al. chose a range of equivalence ratios (0.4–2) and initial pressures (0.2–0.8 atm). This study demonstrated that detonation is stable for equivalence ratios greater than 1.2 for all initial pressures.

Kang et al. [71] investigated supersonic combustion patterns at different equivalence ratios for hydrogen-air mixture in scramjet engines at Mach 7.6 and altitude 31 km. In this study, Kang et al. addressed the effects of fuel equivalence ratios, cavity flame holder, and cowl shape. This study found the equivalence ratios 0.11 and 0.18 provide supersonic combustion and W–shaped cowl provides significant fuel-air mixing. Yeom et al. [72] conducted a three-dimensional numerical simulation to investigate the mixing of the hydrogen-air mixture in a scramjet engine. This investigation was carried by incorporating two sidewalls and a cavity flame holder and did not involve any chemical reactions. It was observed that the sidewalls improve the mixing efficiency. Also, the pressure distribution along the sidewall correlated with the experimental data.

Ebrahimi et al. [73] performed a three-dimensional RANS computation of a cavity exposed to a free-stream Mach number 2 and examined a variety of fuel injection configurations on supersonic combustion. These studies investigated the effect of the cavity in terms of fuel injector location and the injection angle. Ebrahimi et al. concluded that in the case of angled upstream injection, only a small fraction of fuel was entrained into the cavity and vertical injection improved the fuel recirculation. Tatman et al. [74] performed an experimental study of vitiation effects on the flameholding. These tests were performed with different fuels such as hydrogen, ethylene etc. with an inlet Mach number 2. In comparison with the clean air tests, Tatman et al. found a negligible difference. Lee et al. [75] numerically investigated the effects of the fuel injectors and cavity configurations on supersonic combustion using three-dimensional analysis. These studies concluded that a series of fuel nozzle configuration without cavity exhibited better combustor performance when compared with the same configuration with cavity.

Cai et al. [76] numerically studied cavity-based detonation in the supersonic hydrogen-oxygen mixture. Cai et al. compared the simulations of the cavity-based channel with the straight channel. Results showed that the cavity-based channel promoted the detonation initiation and propagation in the supersonic combustible mixture. Also, Cai et al. emphasized that the longer cavities promote the detonation initiation and propagation in the supersonic combustible mixture in a more useful way. Cai et al. [77] further conducted the numerical analysis of the cavity-based detonation using a two-dimensional adaptive mesh model for hydrogen-oxygen mixture with a detailed 32–step chemistry. Results indicated that the blast wave propagation inside the cavity is followed by an oblique shock, the highly unstable shear layers enhanced the mixing effect due to the Kelvin–Helmholtz instability.

The literature review points to the employment of different cavities in conjunction with the instigation mechanism of the detonation engines. Braun et al. [34] presented a parametric study on the possibilities of employing a fluidic valve (with orifice and cavity) for fuel injection. In this study, they employed a series of constant cavity fluidic valves with different orifice geometries and different fuels [34]. This study corroborates the integration of fluidic valve into high-frequency PDEs and RDEs. In an experimental setting, Peace et al. demonstrated the feasibility of the fluidic valve with a plenum cavity of various lengths [35].

CHAPTER 2

METHODOLOGY

2.1 Geometry and Mesh

2.1.1 Geometry

Figure 2.1(a) shows the experimental setup of the fluidic valve attached perpendicular to the side of a PDE toward the exit region. The PDE was 33 in. (838 mm) in length with an inner diameter of 1 in. (25.4 mm). Figure 2.1(b) presents a schematic of the fluidic valve showing various dimensions of the orifice and cavity along with pressure transducer locations. The fluidic valve consisted of a 1/4 in. (6.35 mm) diameter and 1.8 in. (45.7 mm) long orifice connected to a variable-length plenum cavity with a diameter of 3/8 in. (9.525 mm). Pressure transducers (PCB Model 111A24) were mounted at three locations. PCB 5 was located just before the valve orifice inlet which was 25 in. (635 mm) from the upstream end of the PDE. The other two pressure transducers PCB T (located at 95.25 mm length) and PCB B (located at 72.39 mm length) were located in the interior of the valve plenum cavity as shown in Figure 2.1(b).

Two configurations, named as blocked cavity and air injection, were studied. The blocked cavity test was conducted by closing the top of the fluidic valve with end caps or variable plugs of lengths as depicted in Fig. 2.1(b). This resulted in plenum cavity lengths of 2.1 in. (53.34 mm), 2.25 in. (57.18 mm), 2.5 in. (63.5 mm), 2.75 in. (69.85 mm) and 3 in. (76.2 mm) respectively. For the air injection test, the plugs were removed and replaced with variable length injection attachments, thereby providing cavity lengths of 2.1, 2.5 and 3 in. Figure 2.2 shows the air injection attachment of

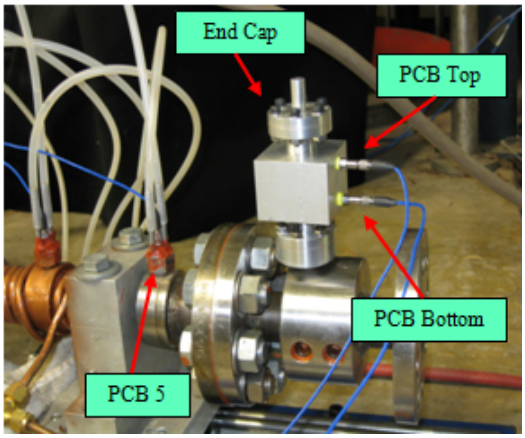

(a) Experimental fluidic valve attached to the PDE

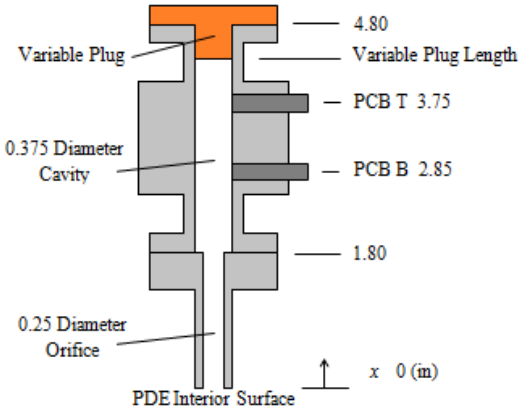

(b) Experimental fluidic valve showing variable plug and pressure transducer arrangement

Figure 2.1: Experimental schematic [35]

pressures 55–95 psia (3.74–6.46 atm)), a 1/4 in. (6.35 mm) gas line attachment and a 1/8 in. (45.7 mm) diameter injector orifice.

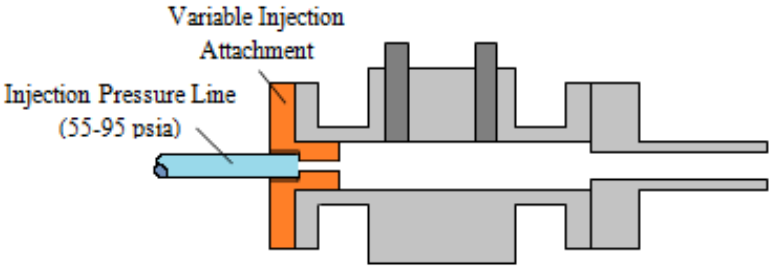

Figure 2.2: Schematic of variable length cavity and the pressure line for injection [35]

Design Modeler is a part of the ANSYS Workbench which is used for creating the model. Also, the created geometry is meshed using ANSYS meshing software. Therefore, ANSYS Workbench was used for the geometry generation. The configuration for the numerical study is a two-dimensional analog of the experimental configuration and is shown in Fig. 2.3. The computational configuration was thought to enable the physics of the wave interactions to be more readily understood without the

complications of a cylindrical valve and the connection between it and the detonation tube. Moreover, instead of the detonation wave propagating over the entire length equivalent of the experiment, which will consume significant computational resources, a shorter domain was considered. This does not affect the gas dynamic properties and the physics associated with the fluidic valve wave interactions. The position of the fluidic valve was altered for the same reason mentioned above.

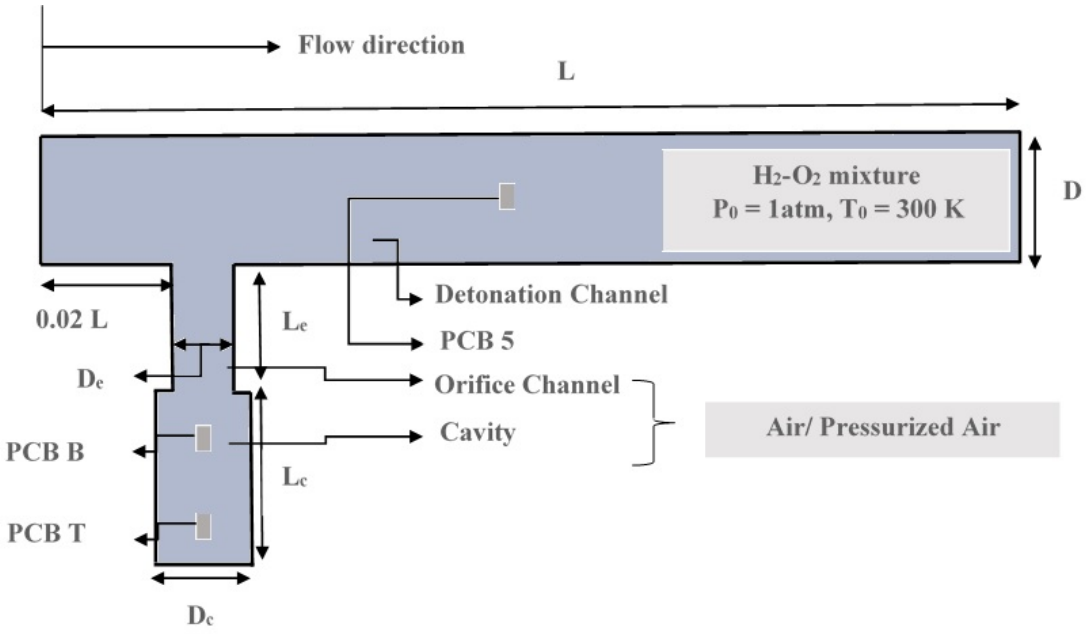

Figure 2.3: Schematic of the computational domain

The main detonation channel has a length $L = 60$ mm and a width of $D = 1.5$ mm. This channel is connected to a cavity with a fixed width of $D_c = 0.57$ mm and a length that varied from $L_c = \{3.18, 3.4, 3.78, 4.16, 4.54\}$ mm via a perpendicular channel with a length of $L_e = 2.72$ mm long and a width of $D_e = 0.38$ mm wide. The combined cavity and the channel form the numerical fluidic valve. The different cavity lengths were to examine the wave interactions, particularly, the pressure buildup to

block the flow. Figure 2.3 shows a cavity that is closed. The cavity itself was located at $0.02L = 1.2$ mm from the upstream end of the detonation channel as shown in Fig. 2.3. This location was chosen and verified that stable detonation was developed before the blast wave enters the fluidic valve.

Similar to the experiments, the pressure histories at three different locations (also labeled PCB 5, PCB B and PCB T) were recorded. PCB 5 was located at $0.4575L$ (located at 27.45 mm length) from the head end of the detonation channel. Within the cavity, PCB B and PCB T were located at $1.5833L_e$ (located at 4.3 mm length) and $2.0833L_e$ (located at 5.6 mm length) from the inlet of the orifice channel as shown in Fig. 2.3.

2.1.2 Mesh

ANSYS Workbench was used for the mesh generation. This geometry (for both PDE duct and the fluidic valve channel) is ideal for the structured mesh. Hence the uniform fine mesh was chosen, shown in Fig. 2.4. This selection also reduced the computational time significantly. For the blocked cavity test and air injection test, for the PDE that was filled with the grid spacing of 0.045–0.055 mm was used. These details are provided in Table 2.1.

Figure 2.4: Mesh generation

Table 2.1: Details of mesh generation

Cavity length mm	Grid spacing mm	Element Type	No. of Nodes	No. of Elements
3.18 mm	0.045 mm	Quadrilateral, Structured	40742	39456
3.40 mm	0.050 mm	Quadrilateral, Structured	39860	38499
3.78 mm	0.045 mm	Quadrilateral, Structured	48736	47214
4.16 mm	0.055 mm	Quadrilateral, Structured	33013	31762
4.54 mm	0.045 mm	Quadrilateral, Structured	49008	47469

The grid spacing of the given range was concluded with the grid dependence study. The results of the grid dependence study are given in section 2.7. From Table 2.1, it can be seen that the different grid spacing was used for different cavity lengths. This was done to get a better solution convergence.

2.2 Governing Equations and Chemical Kinetics

The two-dimensional, reactive Euler equations in Cartesian coordinates were solved. It is known that detonation waves are characterized by a three-dimensional cellular structure [78], [79] which this model lacks to capture. Since the goal of this study is to investigate the shock reflections of the fluidic valve cavity, for the length and time scales of interest, the two-dimensional model was considered to be adequate. The two-dimensional Euler equations can be expressed as

$$\frac{\partial \mathbf{Q}}{\partial t} + \frac{\partial \mathbf{F}}{\partial x} + \frac{\partial \mathbf{G}}{\partial y} = \mathbf{W} \tag{2.1}$$

$$\mathbf{Q} = \begin{bmatrix} \rho \\ \rho V_x \\ \rho V_y \\ \rho E \\ \rho Y_i \end{bmatrix}, \quad \mathbf{F} = \begin{bmatrix} \rho V_x \\ \rho V_x^2 + p \\ \rho V_x V_y \\ \rho E V_x + p V_x \\ \rho V_x Y_i \end{bmatrix}, \quad \mathbf{G} = \begin{bmatrix} \rho V_y \\ \rho V_x V_y \\ \rho V_y^2 + p \\ \rho E V_y + p V_y \\ \rho V_y Y_i \end{bmatrix}, \quad \mathbf{W} = \begin{bmatrix} 0 \\ 0 \\ 0 \\ 0 \\ R_i \end{bmatrix} \tag{2.2}$$

where R_i is the net rate of production of an individual species due to chemical reactions, ρ is the density, p is the pressure, E is the total energy per unit mass and Y_i is the mass fraction of the individual species. Equations of this form are required to model the gas dynamic and chemical reaction coupling inherent to the nature of a self-sustaining detonation wave. The gasdynamic and chemical reaction coupling following a detonation wave is governed both by convection and diffusion [80], [81]. However, past studies have shown that stable detonation solutions can be achieved with the reactive Euler equations and various reaction kinetics where physical diffusion is neglected [82]. This allows for the combustion process to be adequately treated solely with a finite-rate chemistry model. The general form of a chemical reaction is given by equation (2.3). The recombination is being considered with the backward reaction, as some studies neglect this fact.

$$\sum_{i=1}^{N} v'_{i,r} \mathcal{M}_i \underset{k_{b,r}}{\overset{k_{f,r}}{\rightleftharpoons}} \sum_{i=1}^{N} v''_{i,r} \mathcal{M}_i \tag{2.3}$$

The net rate of production of a given species is given by the general law of mass action as equation (2.4). In this form, it is assumed that each individual species source term can be influenced by both the forward and reverse reaction and by third body collisions.

$$R_i = M_{w,i} \sum_{r=1}^{N_R} \Gamma (v''_{i,r} - v'_{i,r}) \left(k_{f,r} \prod_{j=1}^{N} \left[C_{j,r} \right]^{\eta'_{j,r}} - k_{b,r} \prod_{j=1}^{N} \left[C_{j,r} \right]^{v''_{j,r}} \right) \tag{2.4}$$

The forward reaction rate constant is modified Arrhenius rate equation with the temperature dependency and power n. This is given by

$$k_{f,r} = A_r T^n \exp\left(\frac{-E_r}{RT}\right) \tag{2.5}$$

The backward reaction rate is determined by using

$$k_{b,r} = \frac{k_{f,r}}{K_r} \tag{2.6}$$

where the equilibrium constant of each reaction is an expression of the change in Gibbs free energy. The density is computed by the ideal gas law, by assuming a mixture of ideal gases. The specific heat at constant pressure is computed using a mixing law equation (2.7)

$$c_p = \sum Y_i c_{p_i} \tag{2.7}$$

where the specific heat for each individual species as a function of temperature, is computed by use of a two-temperature range piecewise polynomial [83].

A finite-rate chemistry model with a 19–step, reversible elementary mechanism for 8 species was employed for the stoichiometric oxyhydrogen combustion [84]. A finite-rate chemistry model, herein assumes local thermodynamic equilibrium at all instances in time. Implementing a detailed elementary mechanism allows for versatile modeling of hydrogen-based detonations without the need to tune various kinetic parameters or reaction progress variables. The chemical species of consideration include H_2, O_2, H, O, OH, H_2O, HO_2, and H_2O_2. This mechanism is based on a separate kinetic mechanism that was derived for hydrogen combustion and refined to match experimental conditions found within shock tubes and scram jet combustion [58]. Table 2.2 of the appendix shows the Arrhenius parameters for this 19–step kinetic mechanism where the reactions involving N_2 are neglected. This mechanism was successfully used in past studies to determine the influence of partial filling on PDE

performance [17], [85]. This mechanism is based on a separate kinetic mechanism that was derived from hydrogen combustion and refined to match experimental conditions found within shock tubes and scramjet combustion [58], [84].

Table 2.2: H_2–O_2 chemical kinetic mechanism [84]

No	Reaction	A_r [a]	E_r (J/kmol)	n
1	$H_2 + O_2 \rightleftharpoons HO_2 + H$	1.00×10^{11}	2.34×10^{8}	0.00
2	$H + O_2 \rightleftharpoons OH + O$	2.60×10^{11}	7.03×10^{7}	0.00
3	$O + H_2 \rightleftharpoons OH + H$	1.80×10^{7}	3.72×10^{7}	1.00
4	$OH + H_2 \rightleftharpoons H_2O + H$	2.20×10^{10}	2.15×10^{7}	0.00
5	$OH + OH \rightleftharpoons H_2O + O$	6.30×10^{9}	4.56×10^{6}	0.00
6[b]	$H + OH + M \rightleftharpoons H_2O + M$	2.20×10^{19}	0.00	-2.00
7[c]	$H + H + M \rightleftharpoons H_2 + M$	6.40×10^{14}	0.00	-1.00
8[d]	$H + O + M \rightleftharpoons OH + M$	6.00×10^{13}	0.00	-0.60
9[e]	$H + O_2 + M \rightleftharpoons HO_2 + M$	2.10×10^{12}	-4.18×10^{6}	0.00
10	$HO_2 + H \rightleftharpoons OH + OH$	1.40×10^{11}	4.52×10^{6}	0.00
11	$HO_2 + H \rightleftharpoons H_2O + O$	1.00×10^{10}	4.52×10^{6}	0.00
12	$HO_2 + O \rightleftharpoons O_2 + OH$	1.50×10^{10}	3.97×10^{6}	0.00
13	$HO_2 + OH \rightleftharpoons H_2O + O_2$	8.00×10^{9}	0.00	0.00
14	$HO_2 + HO_2 \rightleftharpoons H_2O_2 + O_2$	2.00×10^{9}	0.00	0.00
15	$H + H_2O_2 \rightleftharpoons H_2 + HO_2$	1.40×10^{9}	1.51×10^{7}	0.00
16	$O + H_2O_2 \rightleftharpoons OH + HO_2$	1.40×10^{10}	2.68×10^{7}	0.00
17	$OH + H_2O_2 \rightleftharpoons H_2O + HO_2$	6.10×10^{9}	5.98×10^{6}	0.00
18	$H_2O_2 + M \rightleftharpoons OH + OH + M$	1.20×10^{14}	1.90×10^{8}	0.00
19[f]	$O + O + M \rightleftharpoons O_2 + M$	6.00×10^{10}	-7.53×10^{6}	0.00

[a] Arrhenius pre-exponential factor in units of second, kilomole, m^3.
[b] Third body collision efficiency - $H_2O = 6.0$.
[c] Third body collision efficiency - $H_2O = 6.0$, $H_2 = 2.0$
[d] Third body collision efficiency - $H_2O = 5.0$.
[e] Third body collision efficiency - $H_2O = 16.0$, $H_2 = 2.0$.
[f] Third body collision efficiency - $H_2O = 15.0$.

2.3 Boundary Conditions and Initial Conditions

2.3.1 Boundary Conditions

Figure 2.5 shows the boundary conditions used for the two-dimensional simulations of both blocked cavity and air-injection cases. Boundary condition chosen for the wall closest to the ignition end was adiabatic, slip wall. The detonation wave propagation starts from the head end of the tube and moves towards the right end at supersonic speed. The exit end of the detonation tube is wall boundary condition. The selection of the wall boundary condition does not impact the traversing wave. The wave propagation is affected after the detonation wave is at the end of the tube [17], [35]. This peculiar phenomenon was observed since the waves are governed by Euler equations. The unsteady equations are hyperbolic in nature [86]. Also, as the wave propagates through the combustible mixture, the combusted products are on the far side of the propagating wavefront. The constant pressure boundary condition was chosen for the exit plane of the tube and fluidic valve. When the detonation reaches the open boundary, the pressure just inside the computational domain will suddenly rise to a high value. This creates a large pressure gradient at the exit since the boundary conditions require the flow to relax rapidly to the ambient value. The resulting high flow velocities and over-expansion of the detonation wave results in the decrease of PDE tube pressure to the ambient value. Hence the exit plane of the detonation tube was modeled as a constant pressure boundary condition [67]. For the fluidic valve, with the open boundary, the burnt products will backflow into the PDE tube [67]. In–order–to allow the air or fresh fuel-air mixture into the tube, the constant-pressure boundary condition was chosen. All the other edges of the detonation channel and fluidic valve channel were treated as a wall boundary condition.

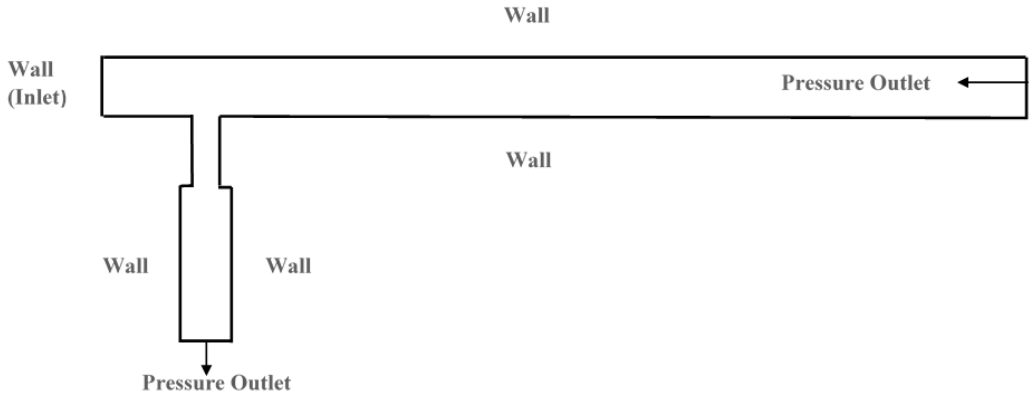

Figure 2.5: Boundary conditions

2.3.2 Initial Conditions

The detonation channel was filled with a stoichiometric oxyhydrogen mixture (mass fraction of hydrogen = 0.888102, mass fraction of oxygen = 0.111898) at an initial pressure of 1 atm and a temperature of 300 K. Deflagration-detonation-transition (DDT) is important to obtain the strong detonation wave propagation. One way to achieve the expedited DDT was by use of detonation wave [87]. Another way to achieve the sustainable wave propagation is to use high pressure and high-temperature conditions for direct ignition. This entails the wavefront to fuel the shock wave. The von Neumann spike is leveraged to initiate the ignition due to the available high pressure [67], [88]. Therefore, wave propagation was initiated with high pressure conditions at high pressure (35 atm) and temperature (3500 K) patched to the first five cells at the head end of the detonation channel as shown in Fig. 2.6. It can be noted that the mass ratios of species in this region were matched with NASA CEA [89] results for a stoichiometric oxyhydrogen mixture as shown in Table 2.3. For all the blocked cavity tests, the fluidic valve was maintained at a constant pressure of 1 atm, temperature of 300 K and air mass fraction as unity. For the air-injection tests, the

fluidic valve was maintained at pressures ranging from 3.7–6.54 atm, temperature of 300 K and air mass fraction as unity.

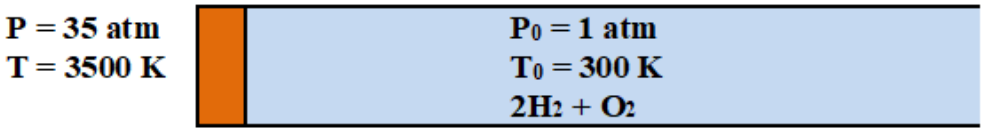

Figure 2.6: Ignition condition

Table 2.3: Mass fraction of species for a stoichiometric H_2–O_2 mixture

Species	Mass Fraction
H_2	0.0225723
O_2	0.106713
H_2O	0.664339
HO_2	0.000424683
H	0.00561757
O	0.0424484
OH	0.157837
H_2O_2	0.000048777

2.4 Numerical Method

ANSYS® Fluent 17.2 was used for the simulations [83]. The two-dimensional planar PDE profile was set up in Fluent. The double-precision solver was used, as this solver exhibited better accuracy than single-precision solvers for the thin and

long channels. Computations for the high-speed compressible flows were carried out with the use of density-based solver. The equations of momentum, energy, species transport, and continuity are also worked out with the aforementioned solver settings [83]. The coupled equations are resolved using either explicit or implicit formulations wherein the first method is comparatively uncomplicated. This ease in solving can be attributed to the method not requiring inputs at each [90]. The explicit and implicit formulations differ in the way the variables are brought to the resolution. The explicit method requires less computational resources as each variable is worked out one cell at a time. On the contrary, the implicit method solves the variables in a parallel fashion and results in expeditious resolution. Chemical reactions for the detonating wavefront transpire in the nanoseconds and explicit methods are more suitable for cases with diminutive time steps. Hence an explicit spatial and transient discretization of the governing equation was chosen. The time step size of 10^{-9} s was chosen for all the simulations. This was chosen based on the results presented in 2.7. This corresponds to a Damköhler number (ratio of convective time scale to the reaction time scale) of unity and a CFL number of 0.1.

A fourth-order Runge–Kutta time integration method was used for the temporal terms. This time-scheme exhibited better results for the density-based solvers using explicit formulation [90]. An AUSM (Advection Upstream Splitting Method) scheme was chosen for computing flux vectors because of its simplicity and accuracy in capturing shock discontinuities [91]. This scheme also enhances the resolution of contact and shock discontinuities [83]. For spatial discretization, a second-order upwind scheme and least squares cell-based gradient has been used. Although detonation is a phenomenon involving viscosity and turbulence, an inviscid flow model was chosen. Since the main goal of this study is to understand the wave interactions

inside the cavity and to obtain qualitative understanding, this selection is justified. The settings for the simulations in Fluent can be found in Table 2.4.

Table 2.4: Fluent settings of CFD simulation

Parameters/Models	Settings
Solver Type	Density-based
Velocity Formulation	Absolute
Time Settings	Transient
Spatial Settings	Planar
Viscous Model	Inviscid
Species Model	Species Transport
Reactions Type	Volumetric
Chemistry Solver	None-Explicit source
Turbulence-Chemistry Interaction	Finite-Rate/No TCI
Mixture Material	Hydrogen–Air
Solution Formulation	Explicit
Flux-Type	AUSM
Spatial Discretization Gradient	Least Squares Cell-Based
Spatial Discretization Flow Solver	Second-Order Upwind
Transient Formulation	Explicit
Time Step, in sec	10^{-9}
Courant Number/ CFL Number	0.1
Solution Initialization	Standard Initialization

2.5 Computational Resource

All the numerical simulations for both blocked cavity cases and air injection cases were run using the Texas Advanced Computing Center (TACC). Detonation simulations with multi-step chemical reactions take excessive computational time.

Hence the Texas Advanced Computing Center's Stampede2 computer cluster was used. Stampede2 was remotely accessed through WinSCP and PuTTY. All file transfers and file downloads were made through a secure connection established by WinSCP while all the commands were given to Stampede2 through PuTTY. After an initial run in the local computer, the relevant case file (.cas), data file (.dat), input file (.jou) along with the bash file (.sh) were transferred to the supercomputer through WinSCP. The input file consists of the information about case file, data file, solver type, courant number, number of time–steps and number of iterations. The bash file contains the information about the nodes, cores and the allocated computational time based on each problem. Using PuTTY, the bash file, which calls the input file was run. By the end of simulation, case files and data files were obtained from WinSCP. These results were post-processed using a local computer.

2.6 Post-Processing

CFD post was used for post-processing the obtained. This software eased the result visualization process.

2.7 Grid Convergence

A consequence of neglecting physical diffusion (discussed in section 2.2) in the governing equations can make the detonation properties grid-dependent [81]. In essence, the detonation wave properties such as wave speed and post-detonation pressure and temperature are influenced by the grid spacing. For this reason, a grid dependency study is carried out to determine the optimal grid spacing that yields acceptable detonation properties for modeling purposes, yet minimizes computational expense. Solutions over a range of different grid resolutions are presented to

demonstrate grid-independent results. For reactive flow simulations, the Damköhler number is defined as the ratio of convective time to the reaction time and should be kept around unity. The reaction time is very small of O(10^{-8}–10^{-10}) s. Hence, the corresponding CFL number approximately varies between 0.1–0.01. For explicit time-stepping schemes, a lower CFL number, typically less than unity, is necessary for proper convergence and stability.

A detailed study was carried out to determine the influence of the time-step on detonation wave properties. For a stoichiometric H_2–O_2, the detonation wave profile characterizes a combined induction and reaction pulse zone mixture of 52 μs [92]. Thus, the grid spacing of interest ranges from 0.01–0.3 mm, which corresponds to a range of 5–0 grid points in the overall reaction zone, respectively [35]. For both time-step sensitivity and grid sensitivity, a tube of 50 mm length and 10 mm diameter were created. The whole tube was filled with a stoichiometric H_2–O_2 mixture at standard temperature and pressure. A shock-induced method for triggering the detonation was utilized 2.6. A region with high pressure of 35 atm and a temperature of 3500 K was patched at the head end of the tube. The mass ratios of the species (2.3) in this region were matched with NASA CEA results for a stoichiometric H_2–O_2 mixture [89].

The effects of time-step on the detonation wave speed are shown in Fig. 2.7. The detonation wave speed converges well with the theoretical CJ velocity of 2836 m/s for a time-step of 10^{-9} s, for almost all grid sizes, considered. The detonation wave speed (U) was calculated using time–of–flight method by choosing two points along the length of the detonation tube, which have the same pressure value at the detonation wave front and their corresponding times. Therefore, a time-step of 10^{-9} s was used for the grid dependence study and for all the subsequent cases. The corresponding CFL number was approximately 0.1 for the time-step of 10^{-9} s.

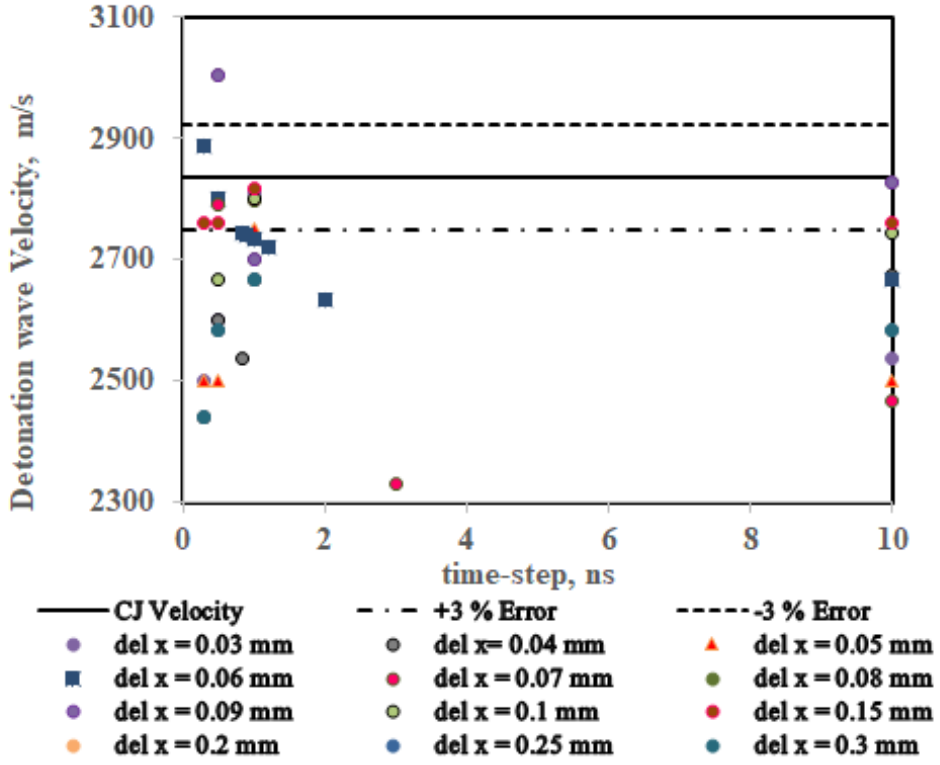

Figure 2.7: Effects of time-step on detonation wave velocity and comparison with CJ velocity

The effects of grid spacing on the detonation wave speed are shown in Fig. 2.8. Previous studies reported that the detonation wave speed becomes strongly dependent on grid spacing at a higher resolution [68]. The detonation wave speed converges well with CJ velocity for the grid spacing ranges from 0.03–0.1 mm. The coarser meshes yielded a lower detonation velocity. It was expected that the wave shape begins to lengthen as the grid spacing increases. Similar phenomena have been reported in previous studies [17], [35], [92]. Further, previous studies showed that the post-detonation temperature appears mostly unaffected by the grid spacing [17], [35]. It was also concluded that a much higher resolution is required to resolve the ZND (Zel'dovich–von Neumann–Döring) detonation wave profile. Hence a CJ detonation wave will be used for this study since the study is considered to be sufficient for

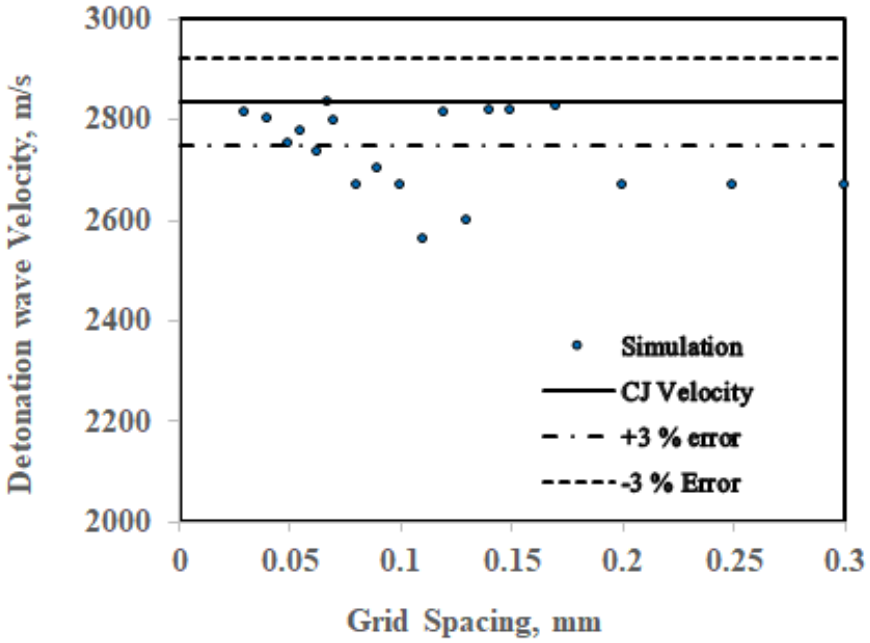

Figure 2.8: Effects of grid spacing on detonation wave velocity and comparison with CJ velocity

studying the fluidic valve operation. The grid spacing of 0.04–0.055 mm yielded a detonation wave speed of 2800 m/s with a post-detonation temperature 3685 K, and a post-detonation pressure of 19 atm which are within 1, −0.27 and 2 percent of theoretical CJ values, respectively. Therefore, a grid spacing of 0.04–0.055 mm was used for all subsequent computations. These results are shown in Table 2.5.

Table 2.5: Deviation of detonation parameters from NASA CEA values

Item	Pressure	Temperature	Velocity
Grid size, 0.045 mm	19 atm	3685 K	2800 m/s
Grid size, 0.050 mm	18.5 atm	3682 K	2893 m/s
Grid size, 0.055 mm	19.1 atm	3691 K	2807 m/s
NASA CEA values	18.657 atm	3675.9 K	2836 m/s
Deviation with CEA values	-1.8-2.3%	-0.24–0.41%	1.02-1.26%

CHAPTER 3

RESULTS

3.1 Blocked Cavity

In the experiment, for these tests, the PDE was operated at 20 Hz allowing multiple detonation wavefronts to pass by the fluidic valve orifice. The fluidic valve was filled with air at ambient conditions, by altering the plenum cavity. The pressure histories at three different locations (labeled PCB 5, PCB B and PCB T) were recorded. Figure 3.1 shows the pressure variation of the incident shock (PCB B) and subsequent reflections inside the fluidic valve for the cavity lengths 3.18, 3.4, 3.78, 4.16 and 4.54 mm (PCB T) for the numerical simulations. For these tests, the fluidic valve was filled with air at ambient conditions. Similar to the experiment, PCB 5 was located at $0.4575L$ from the head end of the detonation channel. Within the cavity, PCB B and PCB T were located at $1.5833L_e$ and $2.0833L_e$ from the inlet of the orifice channel as shown in Fig. 2.3.

It can be observed that with the shortest cavity of length 3.18 mm, the pressure magnitude for the first reflection was 18 atm at 15 μs. Whereas, with the longest cavity of length 4.54 mm, the pressure magnitude for the first reflection was 10 atm at 19 μs. Upon reflection, it can be seen that the peak pressure increased, with the increase being substantially higher for the short cavity. This behavior can be expected from studies of wave reflections in chambers [93]. As this reflected wave traveled back to the PDE, its magnitude decreases with the relative decrease being largest for the shortest cavity. It can be concluded that the plenum cavity length altered the wave reflection pattern and affected the time for which detonation products remained in the

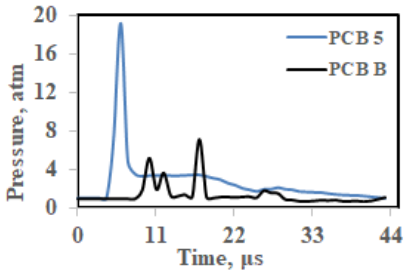

(a) PCB 5 and PCB B trace for 4.54 mm cavity length

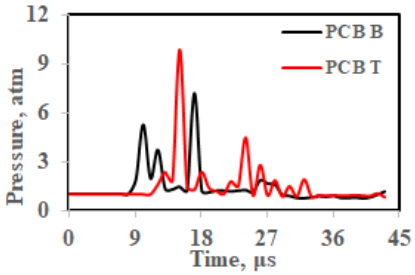

(b) PCB B and PCB T trace for 4.54 mm cavity length

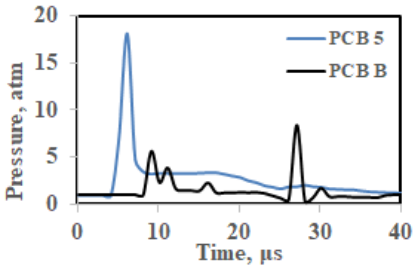

(c) PCB 5 and PCB B trace for 4.16 mm cavity length

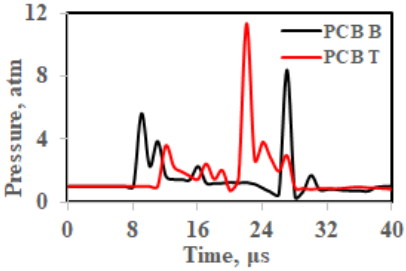

(d) PCB B and PCB T trace for 4.16 mm cavity length

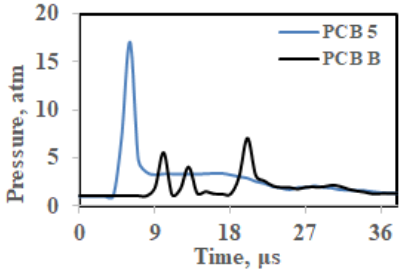

(e) PCB 5 and PCB B trace for 3.78 mm cavity length

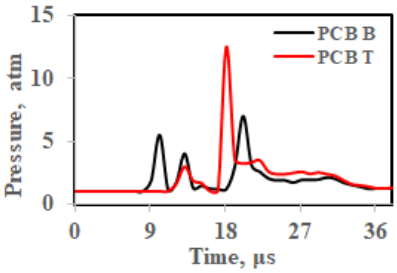

(f) PCB B and PCB T trace for 3.78 mm cavity length

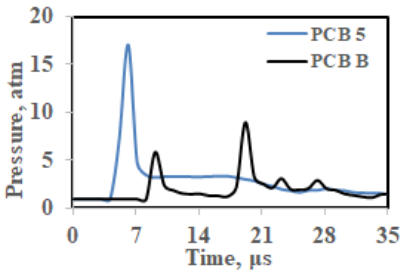

(g) PCB 5 and PCB B trace for 3.4 mm cavity length

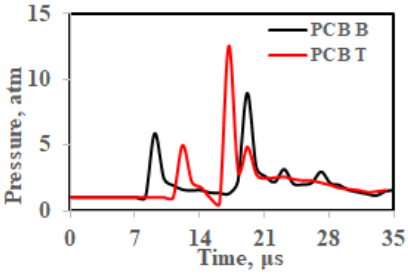

(h) PCB B and PCB T trace for 3.4 mm cavity length

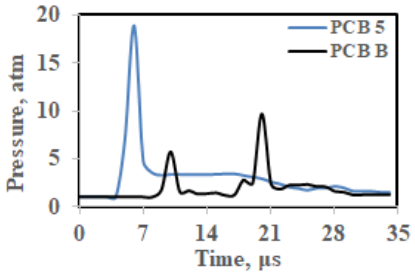

(i) PCB 5 and PCB B trace for 3.18 mm cavity length

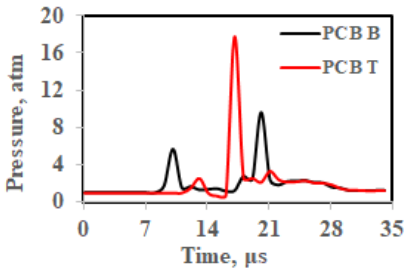

(j) PCB B and PCB T trace for 3.18 mm cavity length

Figure 3.1: Numerical results of pressure variation for a blocked cavity for the lengths specified

cavity. This observation is qualitatively similar to the experiment [35]. The pressure traces show the incident shock passing PCB B (blue trace) and PCB T (red trace) with almost identical forms except for the short time delay.

3.1.1 Analysis

Figures 3.2 and 3.3 show pressure contours of the blast wave reflections inside 3.18 and 4.54 mm long cavities. For the 3.18 mm cavity, the blast wave entered the fluidic valve at 0.003 ms whereas, for 4.54 mm cavity, the blast wave entered the fluidic valve at 0.006 ms. By observation, it is evident that for the longer cavity (4.54 mm), the incident shock wave resided for a longer duration (0.043 ms) than for the duration (0.035 ms) inside the shorter cavity (3.18 mm).

It can be noted that the current simulations were capable of modeling simplified detonation waves, but were not able to resolve the cellular structure. Therefore, the physical structure of the detonation waves was not seen in these figures. However, since this study is targeted toward understanding wave interactions and to obtain qualitative understanding, the lack of resolution was deemed to be acceptable.

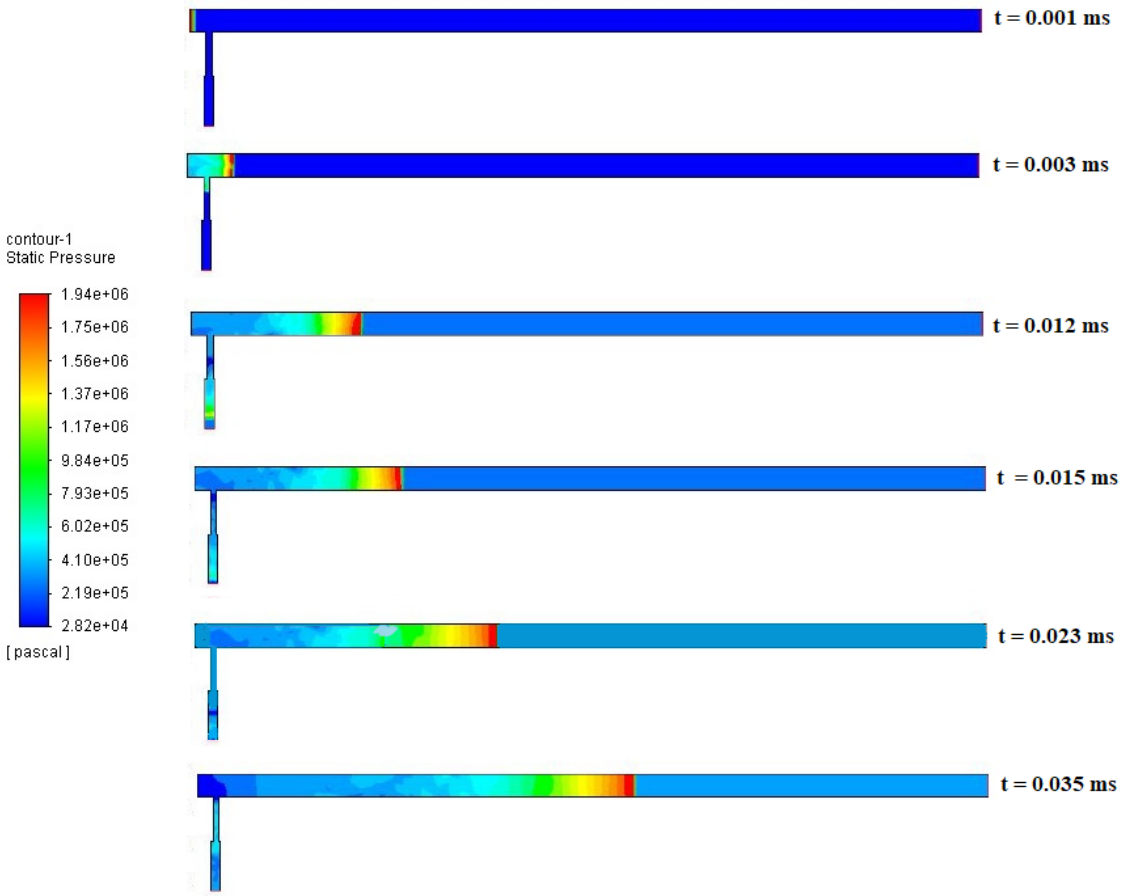

Figure 3.2: Pressure contour for the 3.18 mm long, blocked cavity

Figure 3.4 shows the quasi-one-dimensional representation of the incident shock and subsequent reflections of the experiment [35]. Figure 3.5 shows the time-of-flight representation of the first incident shock wave and the subsequent reflections for the 3.18 and 4.54 mm long cavity lengths. The incident shock and reflections of the highest magnitude from Fig. 3.1 were chosen for the diagram. It is evident that multidimensional reflections occurred between the incident wave and the cavity surfaces. This is due to the manner that the detonation wave entered the cavity from one end. As a result, the incident shock entered the cavity and began to reflect along the cavity walls causing the excess reflections shown in Fig. 3.1. Figures 3.5

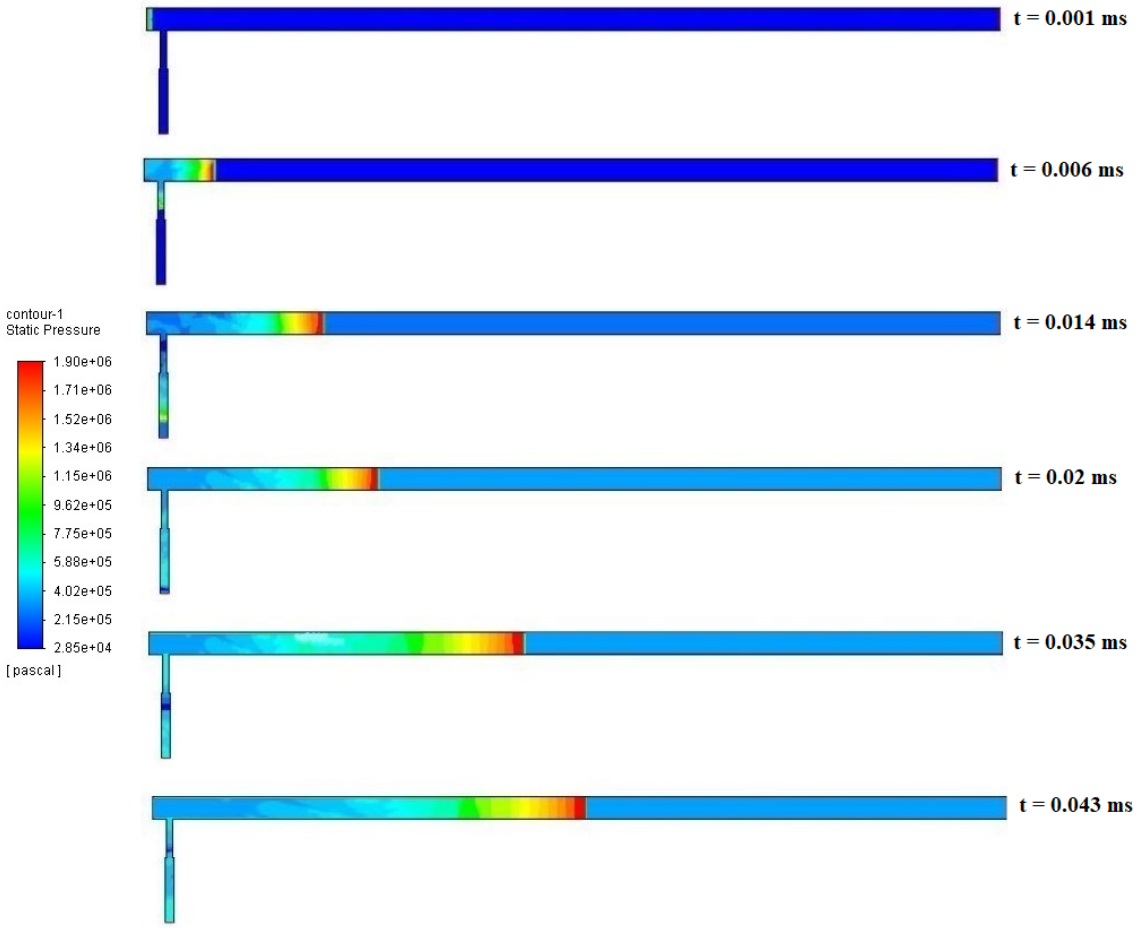

Figure 3.3: Pressure contour for the 4.54 mm long, blocked cavity

show that the cavity length affected the residence time of the incident shock wave inside the cavity. It can be observed that shortening the cavity length affected the manner in which the incident shock propagated and reflected within the cavity. Hence, for longer cavities, the incident shock produced multiple reflections which prolonged the fluidic valve blockage effect. In other words, as the cavity length increases, the incident shock wave induced multiple reflections for a longer duration. While shorter than the experimental valves, as remarked above, these numerical results exhibited qualitatively similar behavior. Similar results were demonstrated by other authors [94].

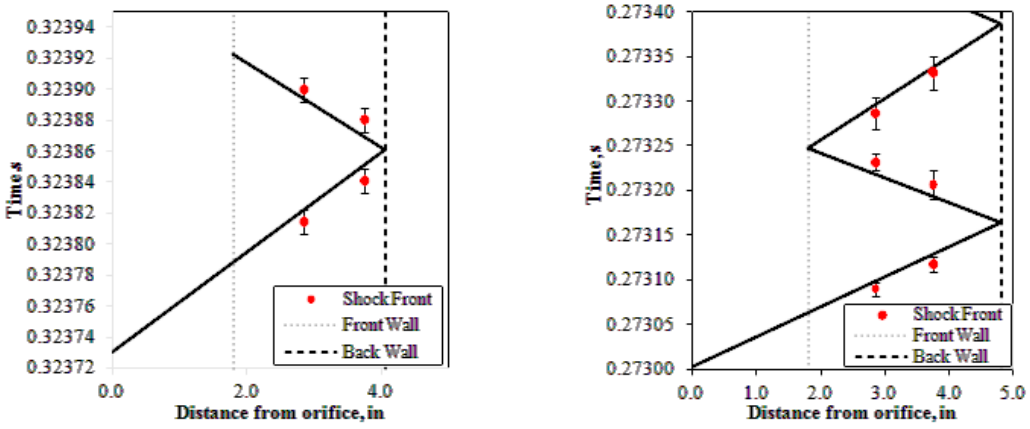

(a) 2.1 in. long cavity (b) 3 in. long cavity

Figure 3.4: Wave diagram of shock reflections within the blocked plenum cavity using experimental data

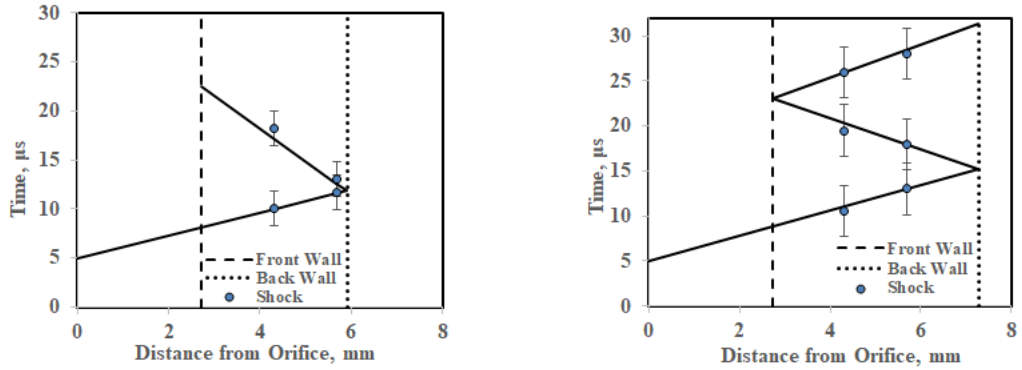

(a) 3.18 mm long cavity (b) 4.54 mm long cavity

Figure 3.5: Time-of-flight representation of the shock reflections for the blocked cavity using numerical data

3.2 Air Injection

Following the blocked cavity tests, high-pressure air at 55–95 psia (3.74–6.46 atm) was introduced in the cavity as indicated in Figs. 3.6-3.8 to simulate the potential fueling conditions of an RDE. Figure 3.1 shows the pressure traces obtained by PCB 5, PCB B, and PCB T measured during typical test runs with injection. It can be noted that the PCB B trace has an initial, steady-state offset due to the injection

pressure conditions. Similar to the blocked cavity tests, the detonation wave entered the fluidic valve cavity but, unlike the blocked cavity tests, exhibited an attenuated reflection behavior as seen in the experiment. This is due to high-pressure air injection as well as a complex wave reflection phenomenon at the contact surface between the air and the detonation products.

Figure 3.6 shows the pressure variation of the incident shock (represented as PCB B) and subsequent reflections inside the fluidic valve for the cavity length 3.18 mm with pressures 3.74, 5.1 and 6.46 atm. For this test, the fluidic valve of length 3.18 mm was filled with air at pressures 3.74, 5.1 and 6.46 atm. In the Fig. 3.6(b) the first reflection pressure was at 11 atm at 8.7 μs. Whereas in Fig. 3.6(f) the first reflection created a spike of 17 atm occurred at 9 μs. It can be concluded that the higher injection pressure led to a higher pressure for the first reflection.

Figure 3.7 shows the pressure variation of the incident shock (represented as PCB B) and subsequent reflections inside the fluidic valve for the cavity length 3.78 mm with pressures 3.74, 5.1 and 6.46 atm. For this test, the fluidic valve of length 3.78 mm was filled with air at pressures 3.74, 5.1 and 6.46 atm. For Fig. 3.6(f), it can be seen that the multiple reflections occurred between 9–15 μs until the injector cavity pressure began to return a steady-state. Whereas, Fig. 3.7(f) depicted that the injector cavity pressure began to return the steady-state at 13 μs. It can be concluded that the longer cavities return earlier to the steady-state than the shorter cavities.

Figure 3.8 shows the pressure variation of the incident shock (represented as PCB B) and subsequent reflections inside the fluidic valve for the cavity length 4.54 mm with pressures 3.74, 5.1 and 6.46 atm. For this test, the fluidic valve of length 4.54 mm was filled with air at pressures 3.74, 5.1 and 6.46 atm. For Fig. 3.8(b), it can be seen that the multiple reflections occurred between 15–22 μs until the injector cavity pressure began to return a steady-state. Whereas, Fig. 3.8(f) depicted that the

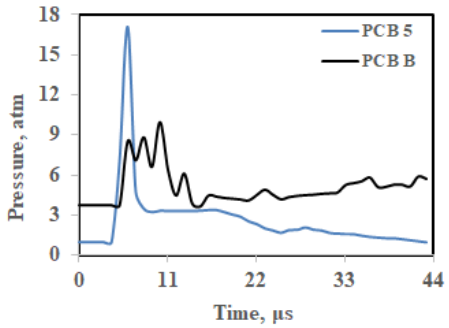

(a) 3.18 mm cavity length with 3.74 atm injection pressure

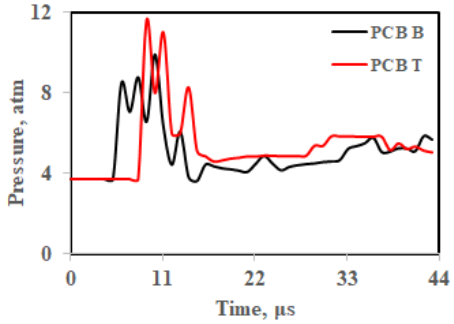

(b) Cavity pressure trace for (a)

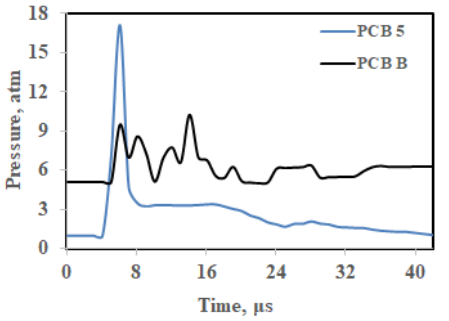

(c) 3.18 mm cavity length with 5.1 atm injection pressure

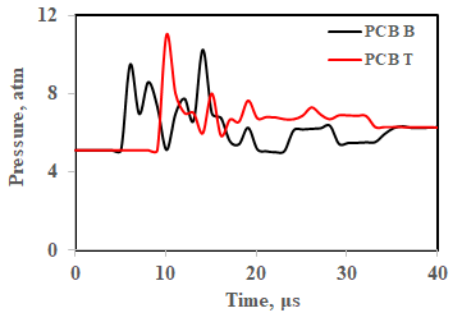

(d) Cavity pressure trace for (c)

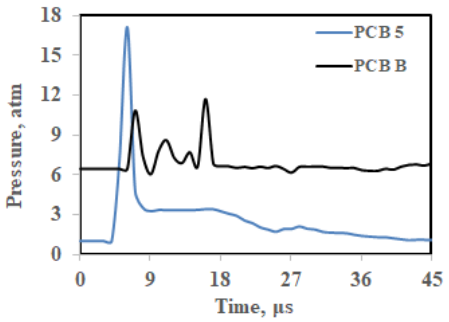

(e) 3.18 mm cavity length with 6.46 atm injection pressure

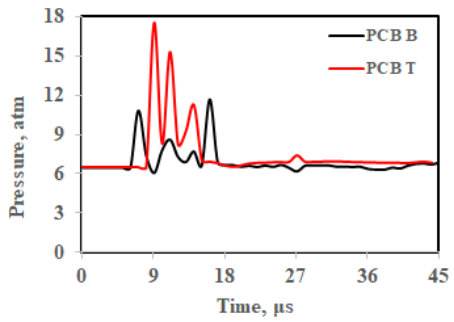

(f) Cavity pressure trace for (e)

Figure 3.6: Numerical results of pressure variation at injection conditions and lengths specified above

injector cavity pressure began to return the steady-state at 18 μs. It can be concluded that the higher injection pressure reduces the number of shock reflections.

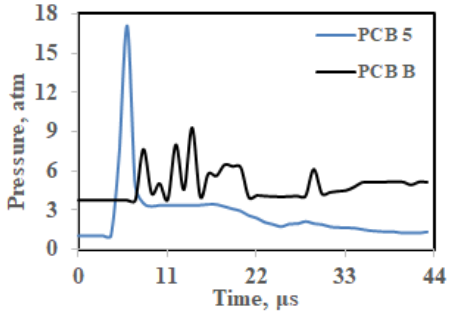

(a) 3.78 mm cavity length with 3.74 atm injection pressure

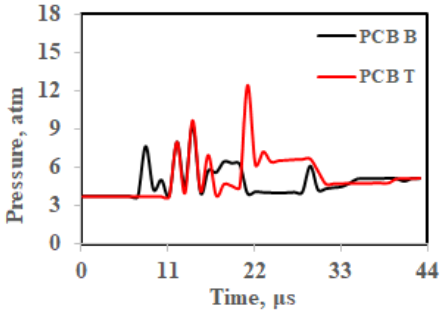

(b) Cavity pressure trace for (a)

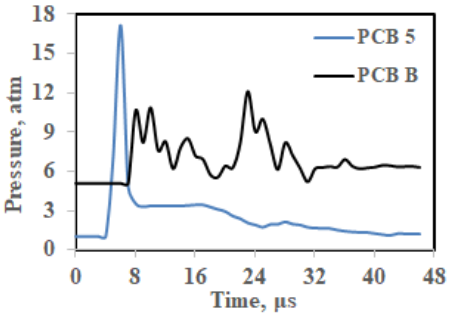

(c) 3.78 mm cavity length with 5.1 atm injection pressure

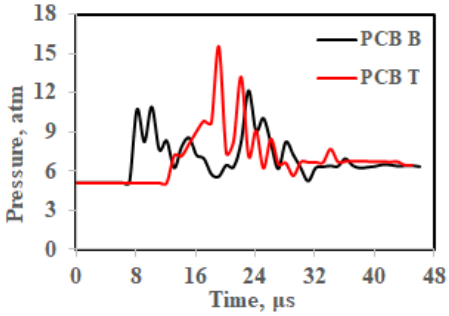

(d) Cavity pressure trace for (c)

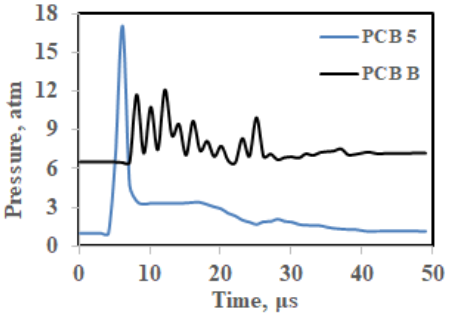

(e) 3.78 mm cavity length with 6.46 atm injection pressure

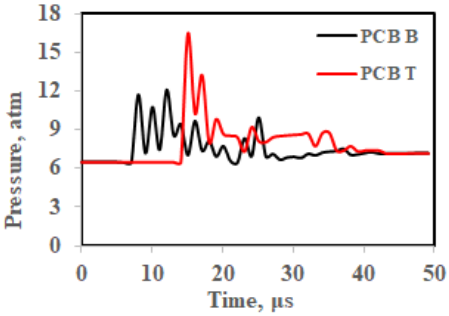

(f) Cavity pressure trace for (e)

Figure 3.7: Numerical results of pressure variation at injection conditions and lengths specified above

For these set of tests, the main concern is the time taken for the injector pressure to return to the steady-state. It is evident that the duration of the wave reflection in the cavity increased with higher initial pressure in the valve. Unlike the blocked

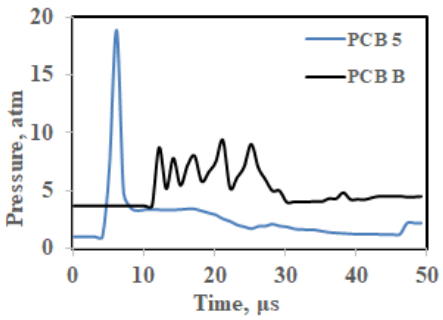

(a) 4.54 mm cavity length with 3.74 atm injection pressure

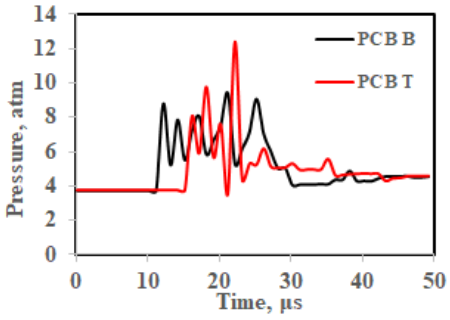

(b) Cavity pressure trace for (a)

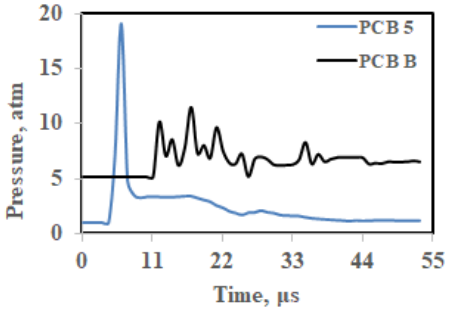

(c) 4.54 mm cavity length with 5.1 atm injection pressure

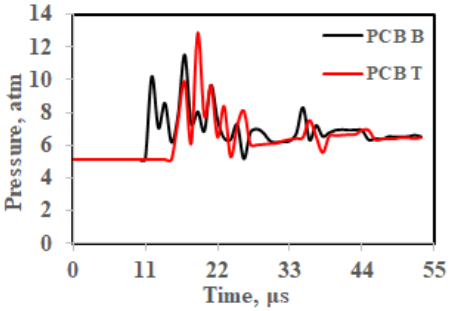

(d) Cavity pressure trace for (c)

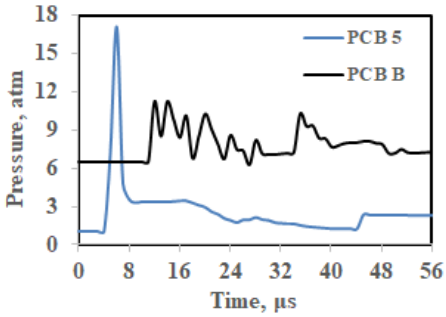

(e) 4.54 mm cavity length with 6.46 atm injection pressure

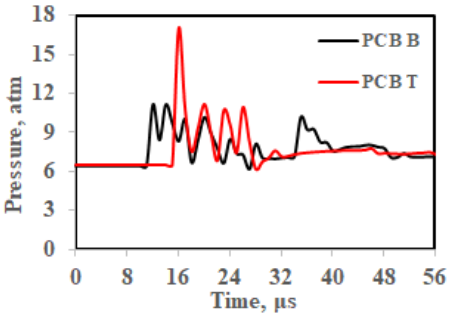

(f) Cavity pressure trace for (e)

Figure 3.8: Numerical results of pressure variation at injection conditions and lengths specified above

cavity, the pressure variation recorded by PCB B (blue trace) and PCB T (red trace) exhibited complex wave behavior arising from the contact surface of the detonation wave and air.

3.2.1 Analysis

Figure 3.9 shows the quasi-one-dimensional wave reflection behavior with pressurized air-injection into the valve. As mentioned earlier, when a detonation wave front past the orifice, a blast wave was diffracted into the plenum cavity, setting up an unsteady wave process. The high-pressure peak from the blast wave blocks the reactants from entering the detonation tube. At a later time, as the trailing edge of the detonation wave propagates past the plenum cavity, the pressure eventually becomes sufficiently weak for the reactants to start flowing into the tube. As can be observed in comparison to the blocked cavity results, the duration of the wave reflection in the cavity increased with air injection pressure. It can be expected that with an increase in injection pressure, the time for which detonation products remained in the cavity would decrease.

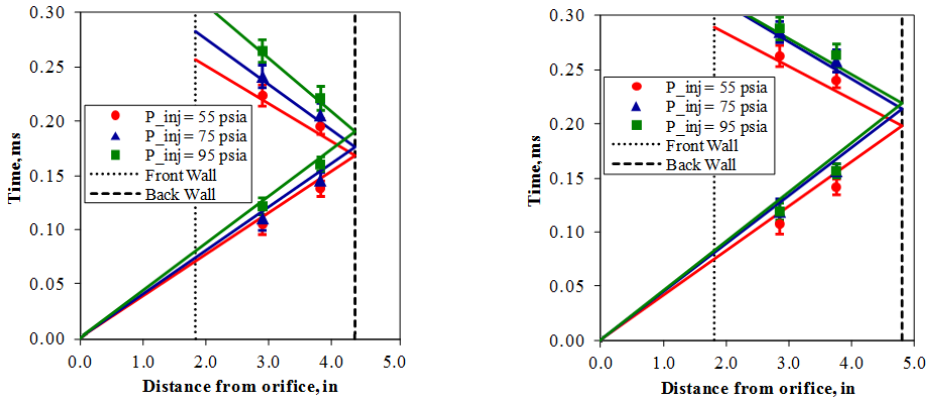

(a) 2.5 in. long cavity (b) 3 in. long cavity

Figure 3.9: Wave diagram of shock reflections within the air-injection plenum cavity using experimental data

Figure 3.10 shows the time-of-flight representation of the first incident shock wave and the subsequent reflections of the cavity lengths 3.78 and 4.54 mm respec-

tively. It can be seen that the duration of the wave reflection in the cavity increased with the air injection pressure. For Fig. 3.10(a), the Mach number of the incident shock for 3.74 atm air injection pressure was 1.34. Whereas, the Mach number of the incident shock for 6.46 atm air-injection pressure is 1.08. For Fig. 3.10(b), the Mach number of the incident shock for 3.74 atm air-injection pressure was 1.616. Whereas, the Mach number of the incident shock for 6.46 atm air-injection pressure was 1.07. Thus, it can be concluded that the Mach number of the incident shock also reduced with the rise of injection pressure. Similar results were demonstrated by Braun et al. [34].

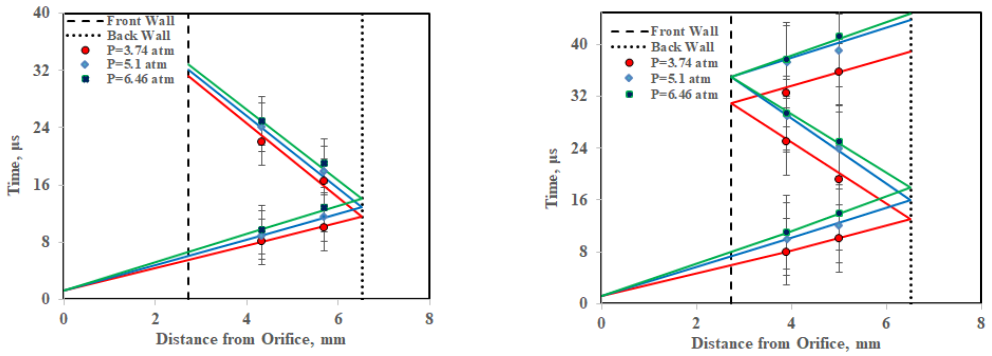

(a) 3.78 mm long cavity

(b) 4.54 mm long cavity

Figure 3.10: Time-of-flight representation of the shock reflections for the air-injection cases based on numerical results

Preliminary data of the post-incident and post-reflected shock pressures are presented in Table 3.1. The results indicate that the long cavity with the highest injection pressure is the most effective for stopping high-pressure, post-detonation gases from entering the valve.

Table 3.1: Post-incident and post-reflected shock pressures in the cavity

Cavity length, mm	Initial cavity pressure, atm	Post-incident shock pressure, atm	Post-reflected shock pressure, atm
3.78	3.74	7–9	11
	5.1	10–12	12–14
	6.46	9–10.5	10–13
4.54	3.74	10–12	12–14
	5.1	10–12	12–13
	6.46	12–13.5	13–18

3.3 Comparison with Experimental Results

A key parameter that governs the allowable operational frequencies of a high-frequency detonation engine, when employing fluidic valves for fuel injections is the interruption time. Figure 3.11 shows an example of the graphical methodology used to determine the interruption time and its uncertainty. The horizontal line indicates the steady-state pressure. The vertical line represents the time at which the detonation wavefront is at its initial value. The oscillatory nature of the pressure, as it passes through the fluidic valve, was tied to the workings of the detonation engine. The red line represents the pressure measured by the pressure transducer B. The gap between the line representative of measurements of PCB B and the dashed line is also known as uncertainty. The gap repeats itself in the area shown between the second set of lines [34].

The chronological difference between the point within the plenum pressure which is at steady state and the point of incidence of the blast wavefront is defined as interruption time [34]. This interruption time could be placed in a non-dimensional form as [34], [95]

$$\tau = \frac{t_{int}}{L_i/U} \tag{3.1}$$

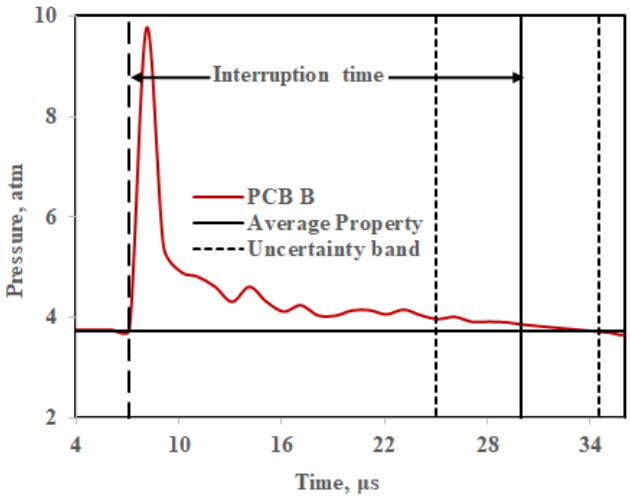

Figure 3.11: Graphical representation of interruption time

where t_{int} is the interruption time, L_i is the distance from the thrust wall of PDE to the beginning of the fluidic valve's orifice, and U is the detonation wave speed. For each experiment, the detonation wave speed U was calculated using the time-of-flight method with the transducers mounted along the main tube [34], [35]. Numerically, the detonation wave speed U was calculated using time-of-flight method by choosing two points along the length of the detonation tube, which have the same pressure value at the detonation wavefront and their corresponding times. Since the steady-state injection pressure was one of the main variables during testing, another non-dimensional term was created by dividing it by the pressure ratio of the detonation [34]. A non-dimensional pressure ratio Π was defined as the ratio of the steady-state injection pressure and the CJ detonation pressure [34]. This parameter can be written as

$$\Pi = \frac{p_p/p_0}{p_{CJ}/p_0} = \frac{p_p}{p_{CJ}} \tag{3.2}$$

where p_p is the plenum cavity injection pressure, and p_{CJ} is the CJ detonation wave pressure predicted by NASA CEA [89] for a stoichiometric detonation mixture.

Figure 3.12 shows the plot of non-dimensional interruption time versus non-dimensional pressure ratio for different cavity lengths (units in mm). Figure 3.12 exhibited an increasing trend of τ with respect to Π. A similar trend was shown in the experimental results. It can be observed that the longer cavities exhibited higher interruption time than the shorter cavities. In other words, the longer cavities took a longer time to return to the steady-state conditions. This is due to the occurrence of multiple reflections. However, the numerical discrepancies in the magnitude of τ with respect to the experimental results appear to have been caused by cavity geometry, position of the fluidic valve, and the viscous effects associated with the experiment.

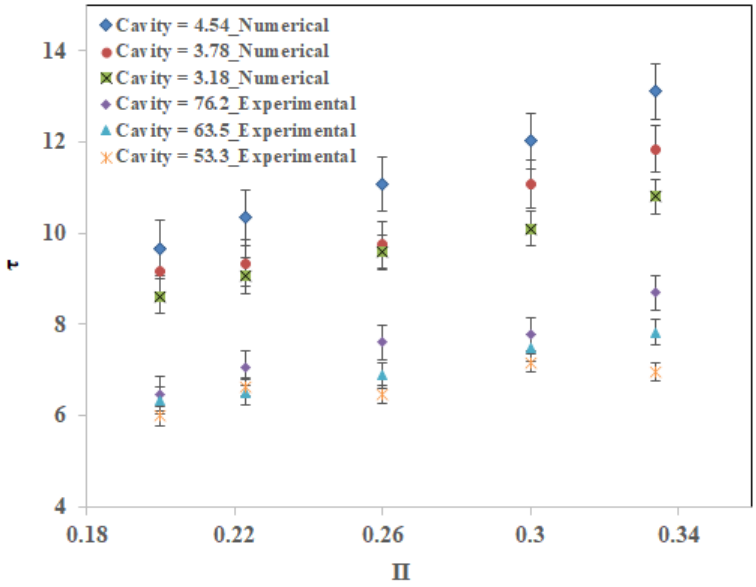

Figure 3.12: Non-dimensional interruption time Vs non-dimensional pressure ratio for different cavity lengths

Figure 3.12 shows the plot of non-dimensional interruption time versus non-dimensional pressure ratio for different fuels. The fluidic valve of the 3.18 mm cavity length was used for this comparison. In Figure 3.13, argon injection portrayed a

decreasing trend for the τ with an increase in Π [34]. Whereas, with the air injection, both the numerical and experimental results [35] exhibited the increasing trend of τ with respect to increasing Π.

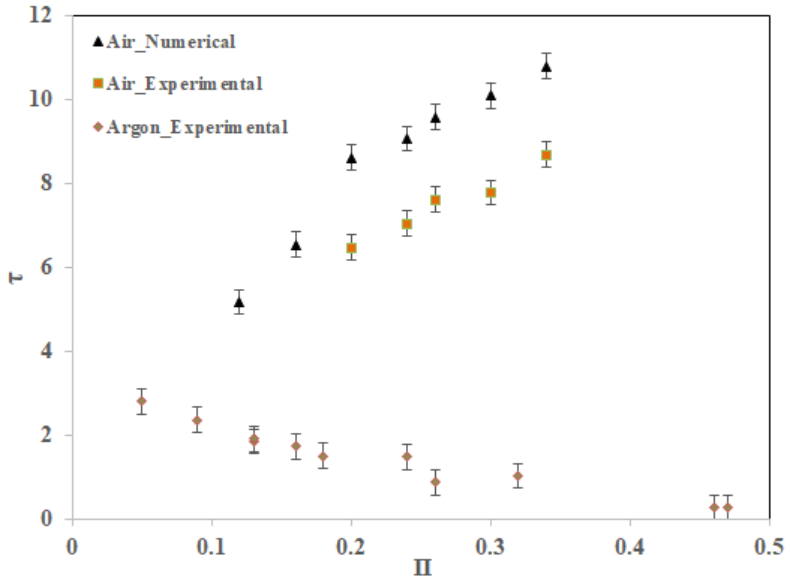

Figure 3.13: Non-dimensional interruption time Vs non-dimensional pressure ratio for different fuels

From equation (3.1), it is evident that the non-dimensional interruption time τ depends on the position of the fluidic valve. Further analysis was conducted to determine the factors impacting the numerical discrepancies observed in the Fig. 3.12. Figure 3.14 shows the schematic of the fluidic valve attached at different lengths of PDE. Two cases, the fluidic valve attached to the PDE at $0.5L$ and the fluidic valve attached to the PDE at $0.8L$ were studied to determine the effects of the position of the fluidic valve.

The cavity geometry is an important design parameter which impacts the performance of the fluidic valve. The optimal geometry of the fluidic valve plenum

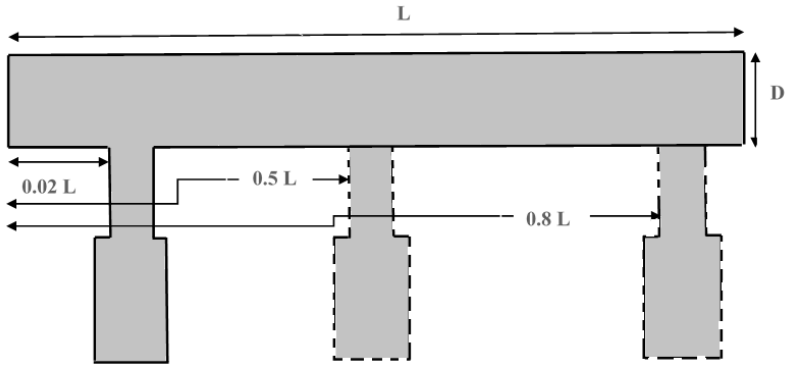

Figure 3.14: Schematic of the fluidic valve attached at different lengths of PDE

cavity was used in the prior computations. The subsequent computations were made by incorporating the experimental fluidic valve geometry. This was done to check the authenticity of the optimal geometry that was used in the earlier computations. Figures 3.15 and 3.16 shows the pressure variation of 53.34 mm cavity when attached to the PDE at different positions as shown. The PDE was 150 mm in length with an inner diameter of 25 mm. The fluidic valve dimensions are shown in Fig. 2.1(b). The pressure history at 72.4 mm length (PCB B) was measured. Similar to the prior cases, the fluidic valve was maintained at a constant pressure of 1 atm, temperature of 300 K and air mass fraction as unity and the detonation channel was filled with a stoichiometric oxyhydrogen mixture (mass fraction of hydrogen = 0.88, mass fraction of oxygen = 0.12) at an initial pressure of 1 atm and a temperature of 300 K. The grid spacing of 0.1 mm was used in these simulations. The fluent settings (shown in Tables 2.4, 2.3) for these simulations are the same as that of previous computations.

From Fig. 3.15, it can be seen that the injector cavity pressure began to return to the cavity injection pressure at 0.35 ms and the pressure peak was recorded as 4.7 atm at 0.28 ms. On the other hand, in Fig. 3.16, the injector cavity pressure takes more time to return to its injection pressure. Also, the pressure peak was recorded as 6.4 atm at 0.06 ms. The change in response of the detonation wave occurs due to

multiple factors. The major sources of variation are the position of the fluidic valve as well as the geometry of the fluidic valve.

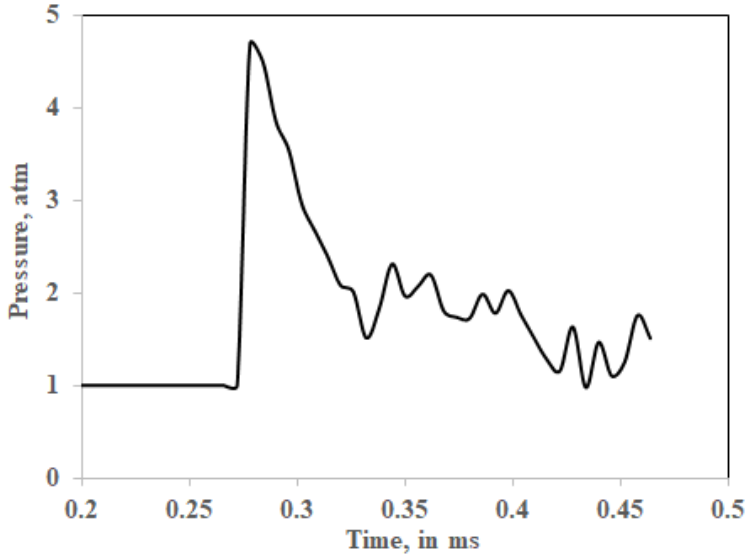

Figure 3.15: Pressure variation of 53.34 mm cavity attached to the PDE at $0.8L$

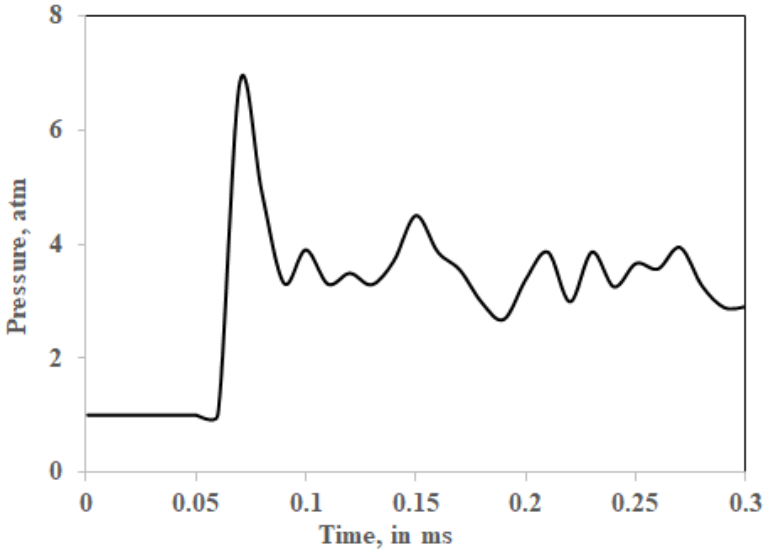

Figure 3.16: Pressure variation of 53.34 mm cavity attached to the PDE at $0.1L$

Figures 3.17 and 3.18 show the pressure contours of 53.34 mm cavity when attached to the PDE at different positions. For the Fig. 3.17, the blast wave entered the orifice at 0.076 ms and reflected at 0.25 ms. Whereas, for Fig. 3.18, the blast wave entered the orifice at 0.04 ms. After 0.09 ms, the wave does not propagate and appears to have settled at that position. From 0.09 ms to 0.14 ms, the cavity pressure took longer to reach the cavity injection pressure and the recorded wave pressure was 3.5 atm and 3.2 atm, respectively. When the fluidic valve (Fig. 2.1(b)) was attached to the PDE at $0.1L$, the cavity pressure took longer to reach its cavity injection pressure along with a large amount of computational expense, when compared to the previous computations (shown in section 3.1 and 3.2). Figures 3.17 and 3.18 help establish the importance of the fluidic valve position with respect to the PDE. This concludes that the numerical discrepancies in the magnitude of τ (shown in Fig. 3.12) with experimental results were limited not only to the viscous effects associated with the experiment but also to the position of the fluidic valve. Further computations were run to determine the effect of the fluidic valve position when the valves were attached at $0.5L$ and $0.8L$ of PDE. For these computations, the geometry mentioned in Fig. 2.3 was utilized to reduce the computational expense. Hence the optimal geometry was employed for further computations by changing the fluidic valve's position.

Figures 3.19 and 3.20 show the plot of non-dimensional interruption time versus non-dimensional pressure ratio for different cavity lengths (units in mm) when the fluidic valve was attached to the PDE at $0.5L$ and $0.8L$, respectively. Similar to the Fig. 3.12, these plots exhibited an increasing trend of τ with respect to Π.

Figure 3.21 compares the experimental findings with the numerical results by using the non-dimensional ratios. For this plot, the shortest cavity of all the cases was chosen. The data points of interruption time for different air injection pressures were joined as a line for visual aid only. Non-dimensional interruption time Vs non-

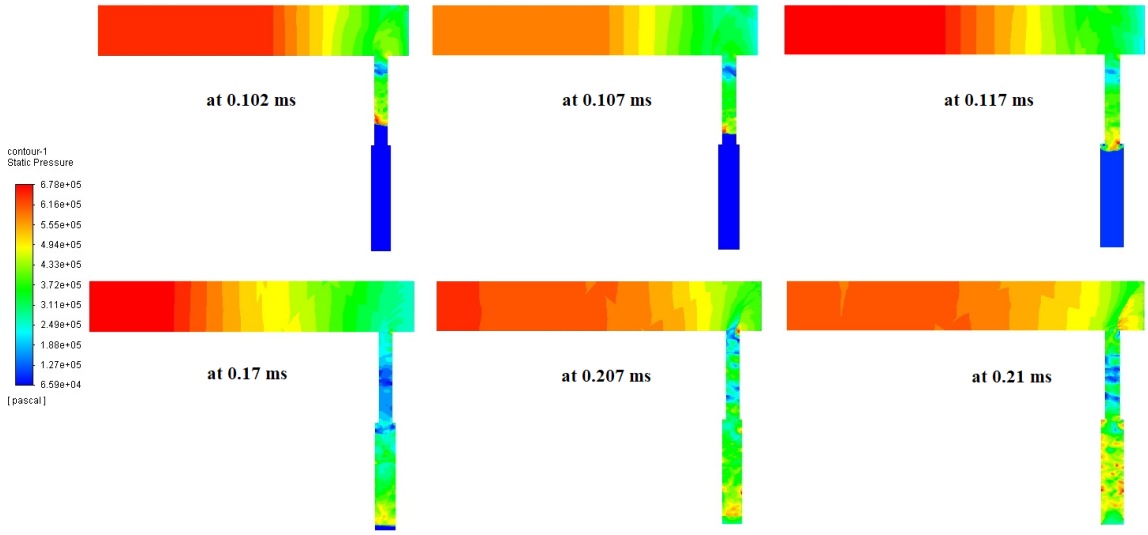

Figure 3.17: Pressure contour of 53.34 mm cavity attached to the PDE at $0.8L$

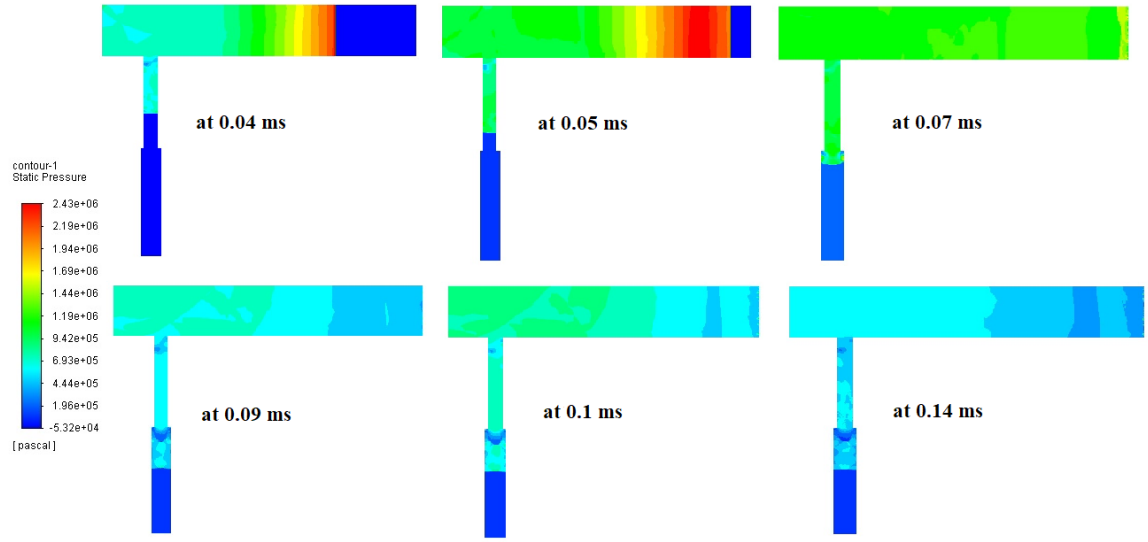

Figure 3.18: Pressure contour of 53.34 mm cavity attached to the PDE at $0.1L$

dimensional pressure ratio for the fluidic valve attached at different lengths of PDE provides a clear trend. The error in the non-dimensional ratio for the fluidic valve when attached at $0.02L$ of PDE was highest among the three test cases at 35 %. The errors in the non-dimensional ratio for the fluidic valve at $0.5L$ and $0.8L$ of the PDE were 12 and 8 %, respectively. In summary, the shorter distance between the thrust

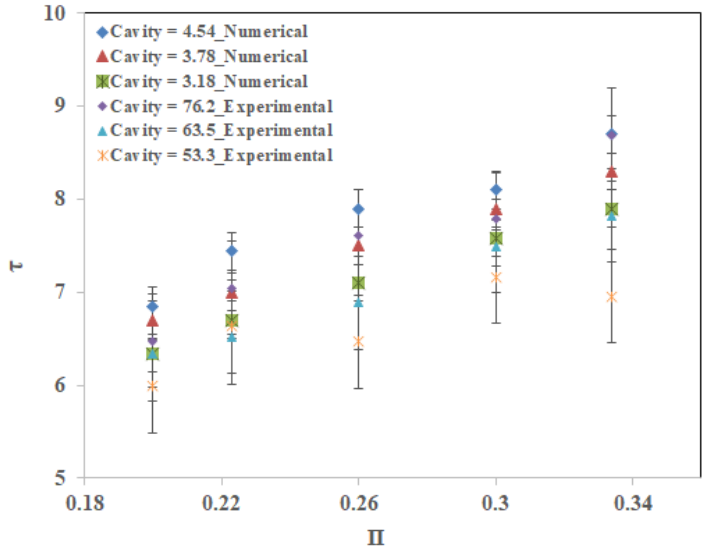

Figure 3.19: Non-dimensional interruption time Vs non-dimensional pressure ratio with the fluidic valve attached at $0.5L$ of PDE

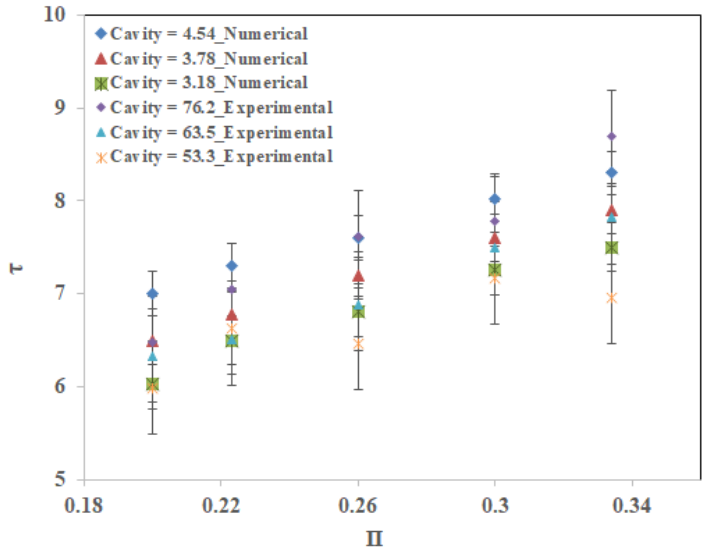

Figure 3.20: Non-dimensional interruption time Vs non-dimensional pressure ratio with fluidic valve attached at $0.8L$ of PDE

wall and the orifice of the fluidic valve, higher the error between experimental and numerical findings. In table A, the non-dimensional interruption time was presented, for all the fluidic valve positions, and a comparison with the experimental values.

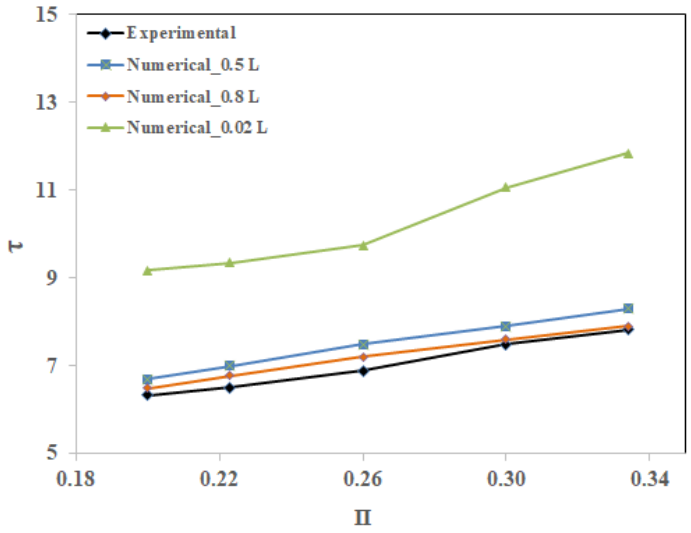

Figure 3.21: Non-dimensional interruption time Vs non-dimensional pressure ratio with the fluidic valve attached at different lengths of PDE

Another important parameter that explains the fluidic valve's performance is the backflow time. Figure 3.22 shows an example to determine the backflow time. The first dashed line represents the time at which the detonation wavefront is at its initial value. The second dashed line represents the time at which the contact surface exit the cavity. The time between these two lines is known as the valve shut-off time, which is defined as the time during which the valve is closed. The backflow time is defined as the time required for the propellants to start propagation after the detonation products exit the plenum cavity. This backflow time helps to predict whether the flow comprises of detonated products or the fresh propellants [34].

The non-dimensional form of backflow time is given in equation (3.3). The backflow time can be measured by plotting the mass fraction of air versus time.

$$\tau_b = \frac{t_b}{L_i/U} \tag{3.3}$$

where, t_b is the interruption time, L_i is the distance from the ignition source to the fluidic valve's orifice, and U is the detonation wave speed.

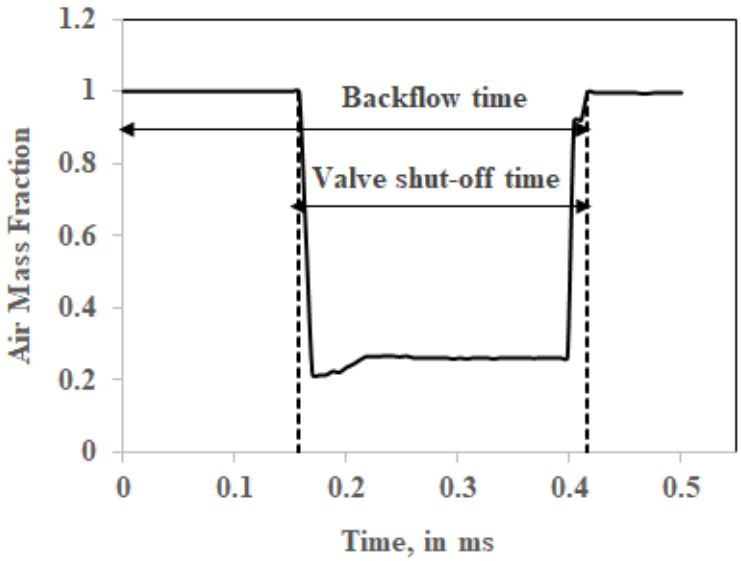

Figure 3.22: Graphical representation of backflow time

Figure 3.23 shows the air mass fraction variation measured at point PCB B for the cavity length 3.18 mm with pressures 3.74, 5.1 and 6.46 atm. For Fig. 3.23(a), the backflow time was 0.15 ms and the valve shut-off time was noted as 0.1 ms. Whereas, for Fig. 3.23(b), the backflow time was 0.23 ms and the valve shut-off time was noted as 0.18 ms. Also, for Fig. 3.23(c), the backflow time was 0.3 ms and the valve shut-off time was noted as 0.2 ms.

Figure 3.24 shows the air mass fraction variation measured at point PCB B for the cavity length 3.78 mm with pressures 3.74, 5.1 and 6.46 atm. For Fig. 3.24(a), the backflow time was 0.2 ms and the valve shut-off time was noted as 0.1 ms. Whereas, for Fig. 3.24(b), the backflow time was 0.24 ms and the valve shut-off time was noted as 0.17 ms. Also, for Fig. 3.24(c), the backflow time was 0.31 ms and the valve shut-off time was noted as 0.2 ms.

Figure 3.25 shows the air mass fraction variation measured at point PCB B for the cavity length 4.54 mm with pressures 3.74, 5.1 and 6.46 atm. For Fig. 3.25(a), the

backflow time was 0.4 ms and the valve shut-off time was noted as 0.23 ms. Whereas, for Fig. 3.25(b), the backflow time was 0.42 ms and the valve shut-off time was noted as 0.24 ms. Also, for Fig. 3.25(c), the backflow time was 0.45 ms and the valve shut-off time was noted as 0.26 ms. From these figures, it is evident that the backflow time follows a similar trend as of interruption time.

Figure 3.26 shows the non-dimensional backflow time versus non-dimensional pressure ratio for different cavity lengths (units in mm). The backflow time followed a similar trend as of interruption time as expected. It can be concluded that the longer cavities exhibited higher backflow time than the shorter cavities. This means, for the longer cavities, the valve shut-off time is greater as those valves takes longer for the recommencement of the propellant flow.

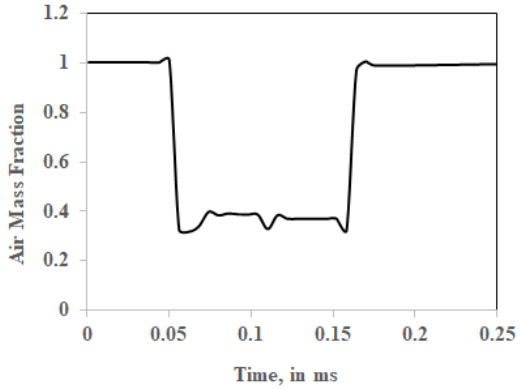

(a) 3.18 mm cavity length with 3.74 atm injection pressure

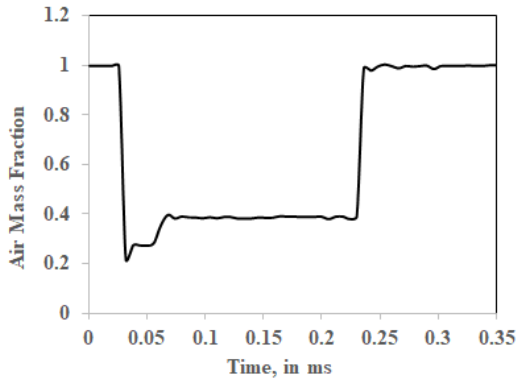

(b) 3.18 mm cavity length with 5.1 atm injection pressure

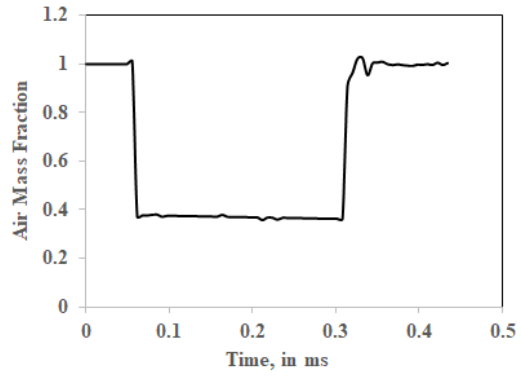

(c) 3.18 mm cavity length with 6.46 atm injection pressure

Figure 3.23: Numerical results of air mass fraction variation at different injection conditions specified above

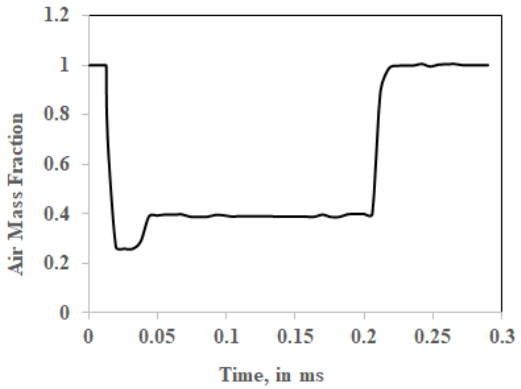

(a) 3.78 mm cavity length with 3.74 atm injection pressure

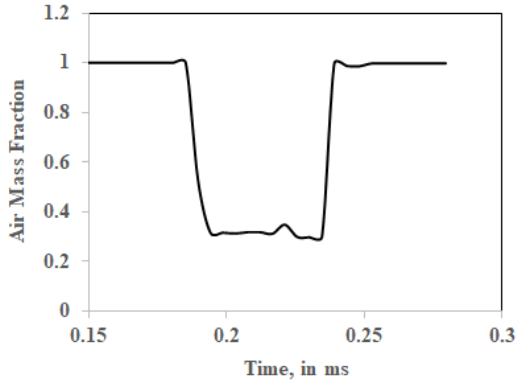

(b) 3.78 mm cavity length with 5.1 atm injection pressure

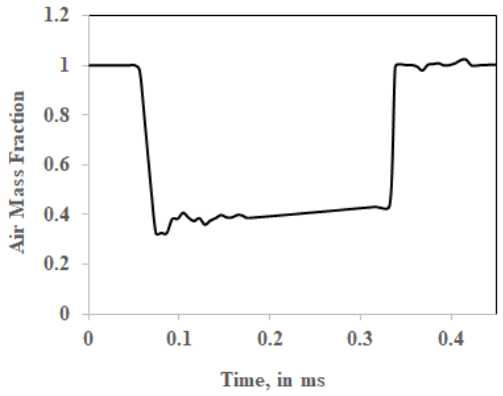

(c) 3.78 mm cavity length with 6.46 atm injection pressure

Figure 3.24: Numerical results of air mass fraction variation at different injection conditions specified above

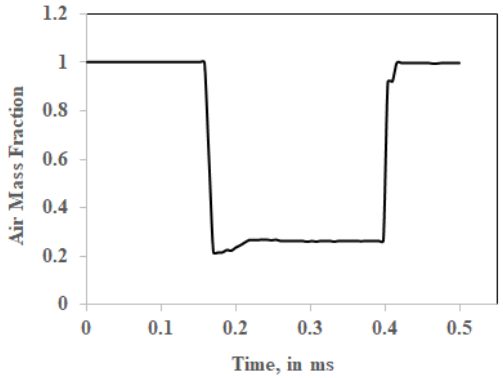

(a) 4.54 mm cavity length with 3.74 atm injection pressure

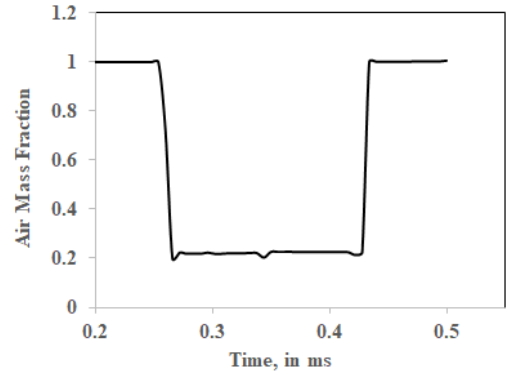

(b) 4.54 mm cavity length with 5.1 atm injection pressure

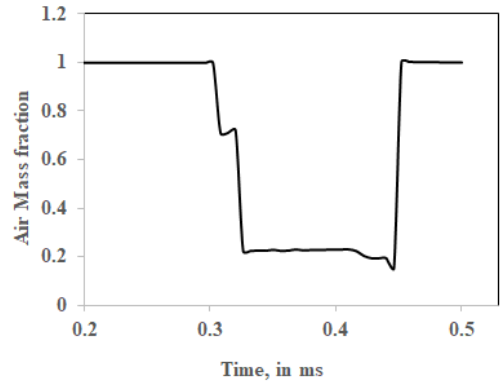

(c) 4.54 mm cavity length with 6.46 atm injection pressure

Figure 3.25: Numerical results of air mass fraction variation at different injection conditions specified above

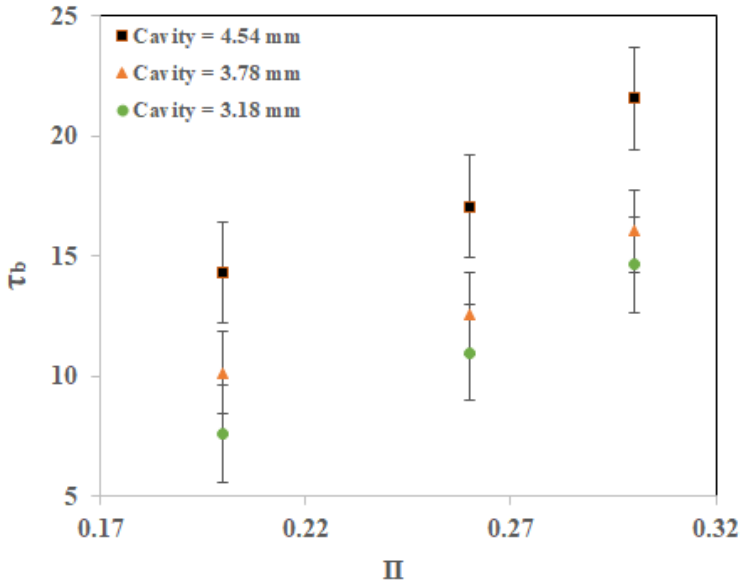

Figure 3.26: Non-dimensional backflow time Vs non-dimensional pressure ratio

CHAPTER 4

CONCLUSIONS AND FUTURE WORK

4.1 Conclusions

The goal of this study was to determine the feasibility of the fluidic valve for integration into high-frequency PDEs and RDEs. The fluidic valve consists of an orifice and cavity. The fluidic valve combines the cavity and injection pressure that utilizes the high pressure of the detonation wave entering the cavity to achieve a controlled interrupted flow. A numerical study of a high-frequency fluidic valve attached to the pulse detonation engine was conducted. The configuration simulated one form of valveless operation of pulse or rotating detonation engines. The two-dimensional inviscid reactive Euler equations and a finite-rate chemistry model were utilized. For stoichiometric oxyhydrogen combustion, eight species, and a 19–step chemical kinetic mechanism were employed. A grid study was performed to identify the most suitable grid spacing and the time-step along with maintaining minimal computational time. It was determined that the grid spacing of 0.04–0.055 mm and the time-step on the order of a nanosecond was best suited for this study. The detonation wave velocity and temperature were 1.26 and 0.32 percent, of theoretical CJ values respectively, for the corresponding grid spacing. The computations were conducted in two phases. The first leg of the computations included fluidic valve with blocked cavity at ambient conditions. The second leg of the computations were conducted with air injected at different pressure from the fluidic valve aperture. Pressure histories were extracted to understand the dynamics and wave interactions inside the plenum cavity. An interruption time was defined and extracted, this determines the time required for the

fluidic valve to return to steady-state injection after the detonation front passes the injector orifice. These results were used for experimental validation. The points below summarize the computational results:

- For the blocked cavity test, the pressure variation corresponds to PCB 5 exhibited a similar trend. Also, the cavity length is directly proportional to the occurrence of reflected waves. The findings were confirmed through analyzing wave diagrams the increase in cavity length culminates into higher reflection pressure.
- The air-injection results indicated that the longer cavities returned earlier to the steady-state conditions than the shorter cavities. The duration of the wave reflection in the cavity increased with higher initial pressure in the valve. These results exhibited complex wave behavior arising from the contact surface of the detonation wave and air.
- For a fluidic valve with active injection, the interruption time depended on the injection pressure ratio. The chosen range of pressure ratios in this work showed an increase in interruption time with an increase in injection pressure ratio. The numerical trends were similar in terms of non-dimensional pressure and interruption time with the experiment but disagreed with earlier single-shot results.
- For a fluidic valve with active injection, the interruption time depended on the distance between the thrust wall and the orifice of the fluidic valve. As the distance between the thrust wall and the orifice increases, for the same fluidic valve, the error of the interruption time increases when compared with the experimental data.

- The backflow time followed a similar trend as of interruption time. For the shorter cavities, the valve shut-off time is greater as those valves take longer for the recommencement of the propellant flow.

4.2 Future Work

The current work touches upon the numerical verification of the experimental findings which included replicating the experimental results using the stoichiometric oxyhydrogen mixture. The proposed future work can build upon the findings of the simulation results by using other combustible mixtures such as hydrogen-air, methane-air, and real gas. The further expansion of air injection computations by using multiple cycles will be helpful in simulating practical scenarios. The current research concluded the importance of the fluidic valve position and the length of the plenum cavity. Future endeavors can confirm the findings of the dissertation by considering the viscous effects and impact of the perturbation on the PDE and fluidic valve operations. Also, the simulations can be performed in the computation domain to capture the impact of using different combustible mixtures in combination with k–ω or k–ϵ models to account for the shear layer impact.

APPENDIX A

NON-DIMENSIONAL DATA COMPARISON AT DIFFERENT FLUIDIC VALVE POSITIONS

Table A.1: Comparison of non-dimensional plots with experimental data

Cavity length, mm	Initial cavity pressure, atm	τ numerical FV at 0.02 L	τ numerical FV at 0.5 L	τ numerical FV at 0.8 L	τ Experimental
3.18	3.74	8.62	6.34	6.02	5.99
	5.1	9.59	7.1	6.8	6.47
	6.46	10.1	7.58	7.25	7.16
3.78	3.74	9.18	6.7	6.5	6.33
	5.1	9.75	7.5	7.2	6.88
	6.46	11.07	7.9	7.6	7.5
4.54	3.74	9.67	6.85	7.01	6.4
	5.1	11.08	7.9	7.6	7.61
	6.46	12.02	8.1	8.03	7.78

APPENDIX B

SHEAR LAYER

This work is not approved by Dr. Frank K. Lu. In the current work, a detonation wave has been modeled as an inviscid two-dimensional a wave propagating through the stoichiometric oxyhydrogen mixture. The propagating wave leaves a trail of combustion products. This shear layer arises due to the presence of an adverse pressure gradient and impacts the wave propagation. Hence, a study of the shear layers and their effect on the wave propagation is explored upon in the current work. The study of these perturbations is very difficult in experiments involving shock tubes. Computational modeling has been found very efficient at picking up the perturbations. In the current work, a detonation wave was modeled as an inviscid two-dimensional wave propagating through the stoichiometric oxyhydrogen mixture. In this study, two cases, an inviscid detonation model and an inviscid model with a small perturbation were studied. The details of these numerical models are given in the section below.

B.1 Numerical model

Using ANSYS Workbench Design Modeler, the detonation channel with a length of $L = 40$ mm and a width of $D = 5$ mm was created. A uniform fine mesh was chosen with a grid spacing of 0.1 mm. The two-dimensional, reactive Euler equations in cartesian coordinates were solved using ANSYS® Fluent 19.2. A finite-rate chemistry model with a 19–step, reversible elementary mechanism for 8 species was employed for the stoichiometric oxyhydrogen combustion (shown in Table 2.2). For both cases, the head end of the channel was closed and treated as an adiabatic, slip wall. The exit plane of the detonation tube was modeled as a constant pressure boundary condition. All the other edges of the detonation channel were treated as a wall boundary condition. For both the cases, the detonation channel was filled with a stoichiometric oxyhydrogen mixture (mass fraction of hydrogen = 0.88, mass fraction

of oxygen = 0.12) at an initial pressure of 1 atm and a temperature of 300 K. For the inviscid detonation case, the ignition was provided by a high pressure (35 atm) and temperature (3500 K) condition patched to the first five cells at the head end of the detonation channel as shown in Fig. 2.6.

For the inviscid detonation with a perturbation case, along with the small patch of the first five cells, a small region near the top and the bottom edges were provided with a high pressure (35 atm), and temperature (3500 K). For the first five cells near the thrust wall, it can be noted that the mass ratios of species were matched with NASA CEA [89] results for a stoichiometric oxyhydrogen mixture as shown in Table 2.3. The Fluent settings for these simulations were given in Table B.1.

B.2 Results and Discussion

The effect of the added perturbation can be seen with the help of pressure, temperature and density plots. These plots were extracted at a point whose length was 20 mm from the head-end of the tube and width was 5 mm. In addition to those plots, the species associated with the strong branching and the weak branching were drawn. The mass fraction plots help to establish the effect of the perturbation based on their activation energies. Figures B.1 and B.2 show the variation of the mass fraction with time for OH and H_2O respectively. From these figures, it can be seen that the effect of the added perturbation was greater for OH. This concludes that the magnitude of OH mass fraction increases for the increases activation energy. This concludes that the shear layer impacts the wave propagation and slows down the flow near the wall of the detonation channel. This scenario matches the analysis made by Massa et al. [96].

Figures B.3, B.4 and B.5 show the variation of pressure, density and temperature with time, respectively. From these figures, it can be seen that both the curves

Table B.1: Fluent settings of shear layer simulation

Parameters/Models	Settings
Solver Type	Density-based
Velocity Formulation	Absolute
Time Settings	Transient
Spatial Settings	Planar
Viscous Model	Inviscid
Species Model	Species Transport
Reactions Type	Volumetric
Chemistry Solver	None-Explicit source
Turbulence-Chemistry Interaction	Finite-Rate/No TCI
Mixture Material	Hydrogen–Air
Solution Formulation	Explicit
Flux-Type	AUSM
Spatial Discretization Gradient	Least Squares Cell-Based
Spatial Discretization Flow Solver	Second-Order Upwind
Transient Formulation	Explicit
Time Step, sec	10^{-9}
CFL Number	0.1
Solution Initialization	Standard Initialization

reach a peak at 0.028 ms. The reduced magnitudes of the peaks in all the curves was due to the shear layer effect. Results obtained in these were retrieved by inducing the viscous effects in the inviscid model. The further verification of the results can be conducted by using the k–ω or k–ϵ turbulent model. This numerical verification has also been proposed as a part of future work. Massa et al.'s discussed the effects of shear layer in gaseous detonation waves [96]. The major distinction in Massa et al. [96] work was by the activation energy and its impact on shear layer formation. The

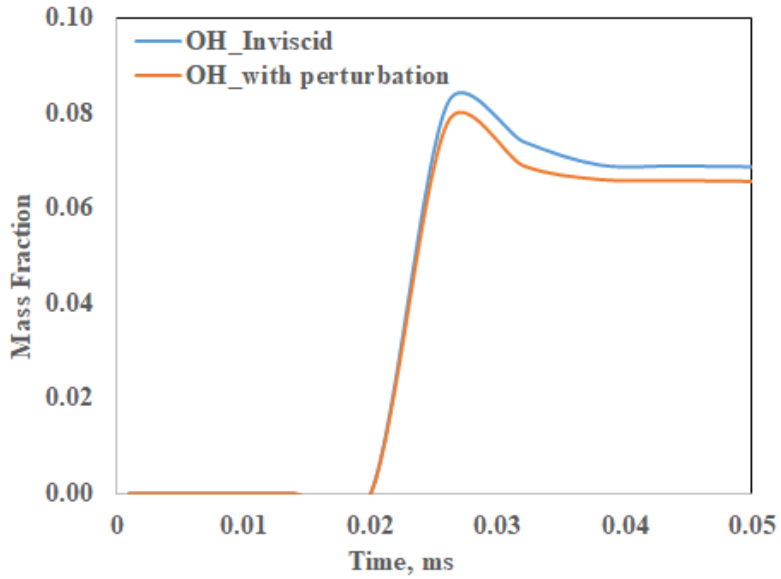

Figure B.1: Mass fraction of OH for oxyhydrogen detonation

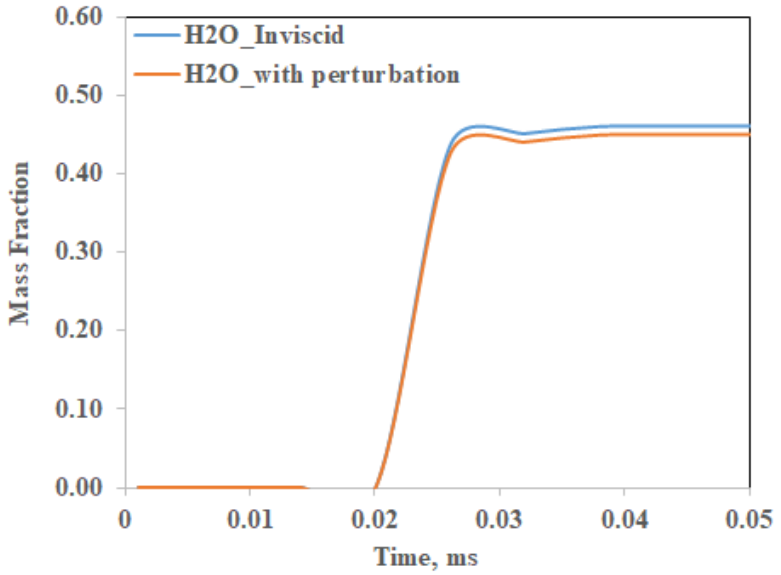

Figure B.2: Mass fraction of H_2O for oxyhydrogen detonation

higher activation energy mixtures appear to have hotspots, whereas the current work appears to lack it.

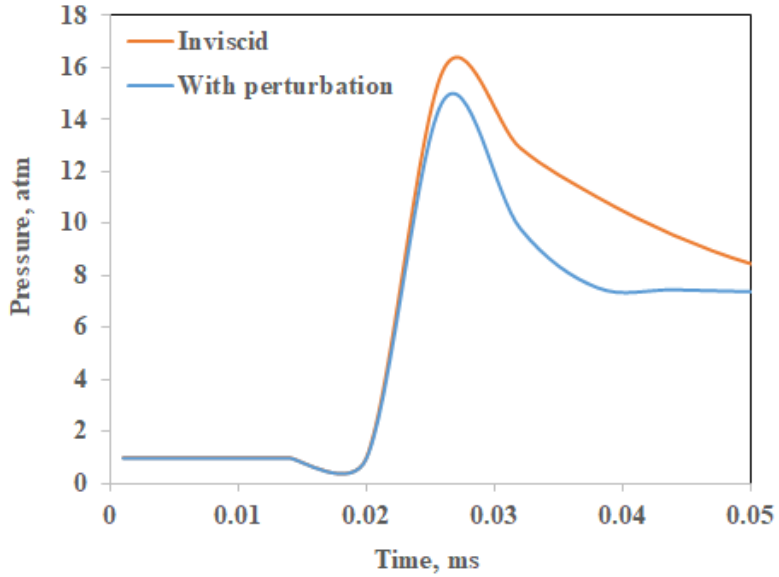

Figure B.3: Pressure variation of oxyhydrogen detonation

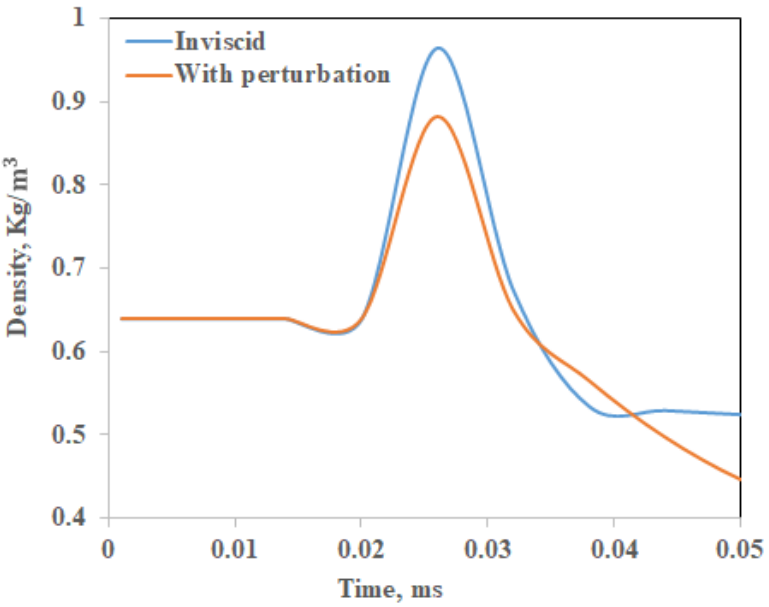

Figure B.4: Density variation of oxyhydrogen detonation

Figure B.6 depicts the pressure contour of the inviscid detonation while considering the effects of the shear layer. The first frame shows the initial formation of

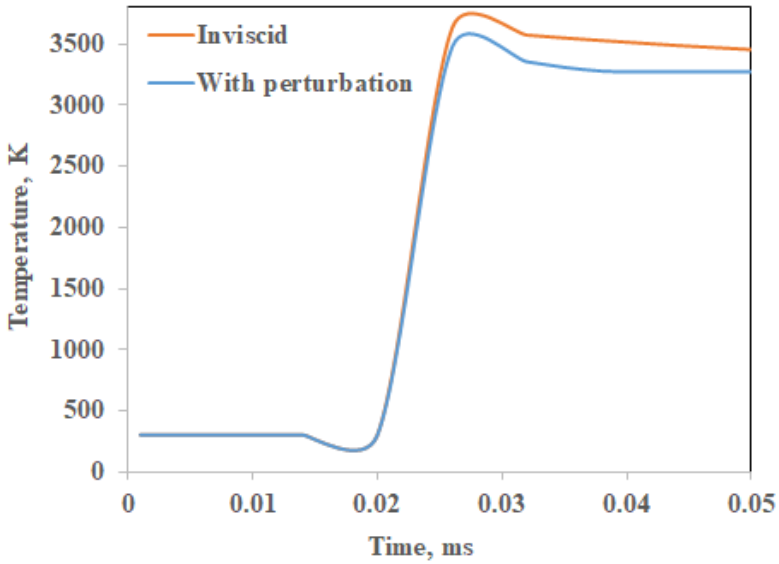

Figure B.5: Temperature variation of oxyhydrogen detonation

the shear layer next to the detonation wavefront. Frame two, three and four show the gradual increase in the shear layer formation. As the wave propagates, the shear layer gets weaker. This might be due to the weak perturbation. Frame 5 displays the dispersion of the shear layer towards the initial position of the wavefront. As the wavefront approaches the exit plane, the shear layer starts consolidating towards the middle of the detonation tube. This can be evidently seen in computational frames 6 and 7. In frame 8, the shear layer converges near the center of the detonation tube and does not seem to have any connection with the boundaries. In frame 9, the shear layer completely disappears as the detonation wavefront nears the exit plane.

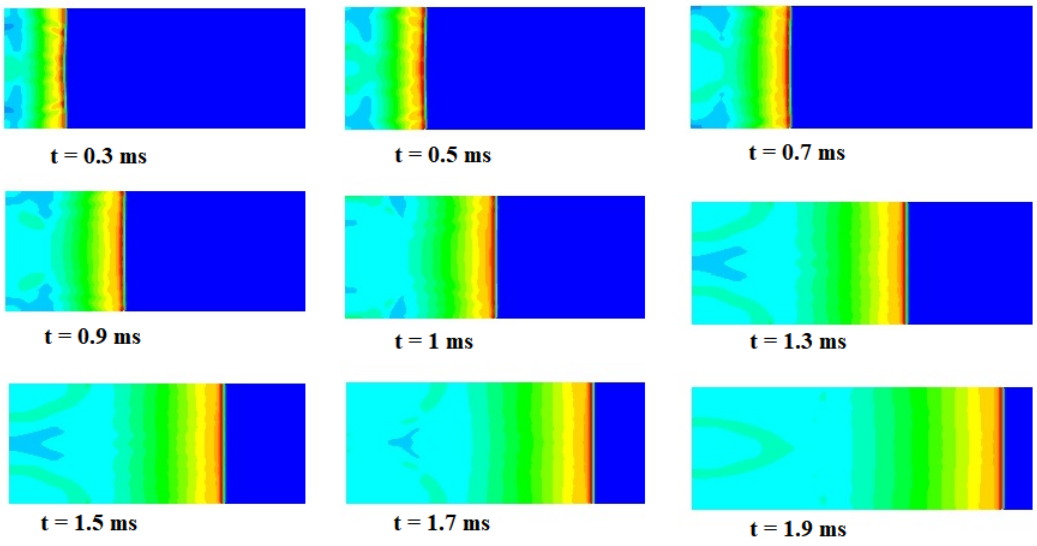

Figure B.6: Pressure contour of the inviscid detonation with perturbation

REFERENCES

[1] P. Wolanski, "Detonative propulsion," *Proceedings of the Combustion Institute*, vol. 34, no. 1, pp. 125–158, 2013.

[2] B. Voitsekhovskii, V. V. Mitrofanov, and M. Topchiyan, "Structure of the detonation front in gases (survey)," *Combustion, Explosion and Shock Waves*, vol. 5, no. 3, pp. 267–273, 1969.

[3] H. W. Nicholls and J. R. B Morrison, "Intermittent detonation as a thrust-producing mechanism," *Journal of Jet Propulsion*, vol. 27, no. 5, pp. 534–541, 1957.

[4] D. R. Wilson and F. K. Lu, "Summary of recent research on detonation wave engines at UTA," in *Proceedings of the International Workshop on Detonation for Propulsion*, 2011.

[5] I. Glassman, R. A. Yetter, and N. G. Glumac, *Combustion*. Academic, 2014.

[6] J. D. Mattingly, *Elements of Propulsion: Gas Turbines and Rockets*. AIAA, 2006.

[7] K. Kailasanath, "Review of propulsion applications of detonation waves," *AIAA Journal*, vol. 38, no. 9, pp. 1698–1708, 2000.

[8] S. Eidelman, W. Grossmann, and I. Lottati, "Review of propulsion applications and numerical simulations of the pulsed detonation engine concept," *Journal of Propulsion and Power*, vol. 7, no. 6, pp. 857–865, 1991.

[9] S. Eidelman and W. Grossmann, "Pulsed detonation engine experimental and theoretical review," in *28th Joint Propulsion Conference and Exhibit*, 1992, p. 3168.

[10] T. Bussing, "Pulse detonation engine theory and concepts," *Progress in Astronautics and Aeronautics*, vol. 165, pp. 421–472, 1996.

[11] K. Kailasanath, "Recent developments in the research on pulse detonation engines," *AIAA Journal*, vol. 41, no. 2, pp. 145–149, 2003.

[12] ——, "The rotating detonation-wave engine concept: A brief status report," in *49th AIAA Aerospace Sciences Meeting Including the New Horizons Forum and Aerospace Exposition*, 2011, p. 580.

[13] G. D. Roy, S. M. Frolov, A. A. Borisov, and D. W. Netzer, "Pulse detonation propulsion: Challenges, current status, and future perspective," *Progress in Energy and Combustion Science*, vol. 30, no. 6, pp. 545–672, 2004.

[14] K. Kailasanath, "Research on pulse detonation combustion systems: A status report," in *47th AIAA Aerospace Sciences Meeting Including the New Horizons Forum and Aerospace Exposition*, 2009, p. 631.

[15] F. K. Lu and E. M. Braun, "Rotating detonation wave propulsion: Experimental challenges, modeling, and engine concepts," *Journal of Propulsion and Power*, vol. 30, no. 5, pp. 1125–1142, 2014.

[16] E. M. Braun, "New detonation concepts for propulsion and power generation," Ph.D Dissertation, The University of Texas at Arlington, Texas, USA, 2012.

[17] A. P. Raghupathy, "A numerical study of detonation and plume dynamics in a pulsed detonation engine," Master's Thesis, University of Cincinnati, Ohio, USA, 2005.

[18] G. Canteins, "A study of continuous rotating detonation with application to propulsion," Ph.D Thesis, University of Poitiers, Poitiers, France, 2006.

[19] F. A. Bykovskii, S. A. Zhdan, and E. F. Vedernikov, "Continuous spin detonations," *Journal of Propulsion and Power*, vol. 22, no. 6, pp. 1204–1216, 2006.

[20] R. Zhou, D. Wu, and J. Wang, "Progress of continuously rotating detonation engines," *Chinese Journal of Aeronautics*, vol. 29, no. 1, pp. 1204–1216, 2016.

[21] J. Kindracki, P. Wolanski, and Z. Gut, "Experimental research on the rotating detonation in gaseous fuels–oxygen mixtures," *Shock Waves*, vol. 21, no. 2, pp. 75–84, 2011.

[22] E. M. Braun, F. K. Lu, D. R. Wilson, and J. A. Camberos, "Airbreathing rotating detonation wave engine cycle analysis," *Aerospace Science and Technology*, vol. 27, no. 1, pp. 201–208, 2013.

[23] C. A. Nordeen, D. Schwer, F. Schauer, J. Hoke, T. Barber, and B. Cetegen, "Thermodynamic model of a rotating detonation engine," *Combustion, Explosion, and Shock Waves*, vol. 50, no. 5, pp. 568–577, 2014.

[24] M. Hishida, T. Fujiwara, and P. Wolanski, "Fundamentals of rotating detonations," *Shock Waves*, vol. 19, no. 1, pp. 1–10, 2009.

[25] T. Fujiwara and S. Tsuge, "Quasi-one dimensional analysis of gaseous free detonations," *Journal of the Physical Society of Japan*, vol. 33, no. 1, pp. 237–241, 1972.

[26] S. Tsuge and T. Fujiwara, "On the propagation velocity of a detonation-shock combined wave," *ZAMM-Journal of Applied Mathematics and Mechanics/Zeitschrift für Angewandte Mathematik und Mechanik*, vol. 54, no. 3, pp. 157–164, 1974.

[27] J. A. Nicholls and R. E. Cullen, "The feasibility of a rotating detonation wave rocket motor," Michigan University Ann Arbor College of Engineering, Tech. Rep., 1964.

[28] F. A. Bykovskii and E. F. Vedernikov, "Self-sustaining pulsating detonation of gas-mixture flow," *Combustion, Explosion and Shock Waves*, vol. 32, no. 4, pp. 442–448, 1996.

[29] F. A. Bykovskii and V. Mitrofanov, "Detonation combustion of a gas mixture in a cylindrical chamber," *Combustion, Explosion and Shock Waves*, vol. 16, no. 5, pp. 570–578, 1980.

[30] F. Bykovskii, "Thermal fluxes in combustion chamber walls in the detonation and turbulent combustion modes," *Combustion, Explosion and Shock Waves*, vol. 27, no. 1, pp. 66–71, 1991.

[31] A. R. Mizener and F. K. Lu, "Low-order parametric analysis of a rotating detonation engine in rocket mode," *Journal of Propulsion and Power*, vol. 33, no. 6, pp. 1543–1554, 2017.

[32] T. H. Yi, J. Lou, C. Turangan, J. Y. Choi, and P. Wolanski, "Propulsive performance of a continuously rotating detonation engine," *Journal of Propulsion and Power*, vol. 27, no. 1, pp. 171–181, 2011.

[33] D. Schwer and K. Kailasanath, "Numerical investigation of the physics of rotating-detonation-engines," *Proceedings of the Combustion Institute*, vol. 33, no. 2, pp. 2195–2202, 2011.

[34] E. M. Braun, T. S. Balcazar, D. R. Wilson, and F. K. Lu, "Experimental study of a high-frequency fluidic valve fuel injector," *Journal of Propulsion and Power*, vol. 28, no. 5, pp. 1121–1125, 2012.

[35] J. T. Peace, D. D. Joshi, and F. K. Lu, "Experimental study of high-frequency fluidic valve injectors for detonation engine applications," AIAA Paper 2014–1318, 2014.

[36] W. J. M. Rankine, "On the thermodynamic theory of waves of finite longitudinal disturbance," *Philosophical Transactions of the Royal Society of London*, vol. 160, pp. 277–288, 1870.

[37] H. Hugoniot, P, "Memoire sur la propagation du movement dans les corps et plus specialement dans les gaz prfaits premiere partie," *Journal De Lecole Polytechnique*, vol. 57, pp. 3–97, 1887.

[38] D. L. Chapman, "On the rate of explosion in gases," *The London, Edinburgh, and Dublin Philosophical Magazine and Journal of Science*, vol. 47, no. 284, pp. 90–104, 1899.

[39] E. Jouguet, "Sur la propagation des réactions chimiques dans les gaz," *J. Maths. Pure Appl.*, vol. 7, p. 347, 1905.

[40] Y. B. Zeldovich, "K teori rasprostranenia detonazi v gasoobrasnikh systemakh," *Zhurnal Experimentalnoi i Teoreticheskoi Fiziki*, vol. 10, no. 5, pp. 542–568, 1940.

[41] J. von Neumann, "Theory of detonation waves: Progress report to the National Defense Research Committee Div. B, OSRD-549,(April 1, 1942. PB 31090)," *John Von Neumann: Collected Works*, vol. 1957, 1903.

[42] W. Döring, "Über den detonationsvorgang in gasen," *Annalen der Physik*, vol. 435, no. 6-7, pp. 421–436, 1943.

[43] W. Fickett and W. C. Davis, *Detonation: Theory and Experiment*. Courier Corporation, 2000.

[44] F. Pintgen, C. Eckett, J. Austin, and J. Shepherd, "Direct observations of reaction zone structure in propagating detonations," *Combustion and Flame*, vol. 133, no. 3, pp. 211–229, 2003.

[45] F. Ma, J.-Y. Choi, and V. Yang, "Thrust chamber dynamics and propulsive performance of single-tube pulse detonation engines," *Journal of Propulsion and Power*, vol. 21, no. 3, pp. 512–526, 2005.

[46] C. Li and K. Kailasanaath, "A numerical study of reactive flows in pulse detonation engines," in *37th Joint Propulsion Conference and Exhibit*, 2001, p. 3933.

[47] X. He and A. R. Karagozian, "Numerical simulation of pulse detonation engine phenomena," *Journal of Scientific Computing*, vol. 19, no. 1-3, pp. 201–224, 2003.

[48] C. Westbrook, F. Dryer, and K. Schug, "Chemical kinetics and modeling of combustion," *The Combustion Institute, Pittsburgh, PA*, vol. 749, 1981.

[49] R. Yetter, F. Dryer, and H. Rabitz, "A comprehensive reaction mechanism for carbon monoxide/hydrogen/oxygen kinetics," *Combustion Science and Technology*, vol. 79, no. 1-3, pp. 97–128, 1991.

[50] W. Fickett and W. W. Wood, "Flow calculations for pulsating one-dimensional detonations," *The Physics of Fluids*, vol. 9, no. 5, pp. 903–916, 1966.

[51] J. J. Erpenbeck, "Stability of idealized one-reaction detonations," *The Physics of Fluids*, vol. 7, no. 5, pp. 684–696, 1964.

[52] G. Abouseif and T.-Y. Toong, "Theory of unstable one-dimensional detonations," *Combustion and Flame*, vol. 45, pp. 67–94, 1982.

[53] L. He and J. H. Lee, "The dynamical limit of one-dimensional detonations," *Physics of Fluids*, vol. 7, no. 5, pp. 1151–1158, 1995.

[54] S.-T. Yu, S.-C. Chang, P. Jorgenson, S.-J. Park, and M.-C. Lai, "Basic equations of chemically reactive flows for computational fluid dynamics," in *36th AIAA Aerospace Sciences Meeting and Exhibit*, p. 1051.

[55] B. Sekar, S. Palaniswamy, O. Peroomian, and S. Chakravarthy, "A numerical study of the pulse detonation wave engine with hydrocarbon fuels," in *34th AIAA/ASME/SAE/ASEE Joint Propulsion Conference and Exhibit*, 1998, p. 3880.

[56] T. Bussing and G. Pappas, "An introduction to pulse detonation engines," in *32nd Aerospace Sciences Meeting and Exhibit*, 1994, p. 263.

[57] J. Clutter and W. Shyy, "Evaluation of source term treatments for high-speed reacting flows," in *36th AIAA Aerospace Sciences Meeting and Exhibit*, 1998, p. 250.

[58] C. J. Jachimowski, "An analytical study of the hydrogen-air reaction mechanism with application to scramjet combustion," NASA TP-2791, 1988.

[59] H. Shang, Y. Chen, P. Liaw, C. Chen, and T. Wang, "Investigation of chemical kinetics integration algorithms for reacting flows," in *33rd Aerospace Sciences Meeting and Exhibit*, 1995, p. 806.

[60] G. Moretti, "A new technique for the numerical analysis of nonequilibrium flows," *AIAA Journal*, vol. 3, no. 2, pp. 223–229, 1965.

[61] K. Hsu and A. Jemcov, "Numerical investigations of detonation in premixed hydrogen-air mixture-assessment of simplified chemical mechanisms," in *Fluids 2000 Conference and Exhibit*, 2000, p. 2478.

[62] A. K. Varma, A. U. Chatwani, and F. V. Bracco, "Studies of premixed laminar hydrogen-air flames using elementary and global kinetics models," *Combustion and Flame*, vol. 64, no. 2, pp. 233–236, 1986.

[63] R. Rogers and W. Chinitz, "Using a global hydrogen-air combustion model in turbulent reacting flow calculations," *AIAA Journal*, vol. 21, no. 4, pp. 586–592, 1983.

[64] S. Vajda, H. Rabitz, and R. Yetter, "Effects of thermal coupling and diffusion on the mechanism of h2 oxidation in steady premixed laminar flames," *Combustion and Flame*, vol. 82, no. 3-4, pp. 270–297, 1990.

[65] G. Kistiakowsky and P. Kydd, "Gaseous detonations. ix. a study of the reaction zone by gas density measurements," *The Journal of Chemical Physics*, vol. 25, no. 5, pp. 824–835, 1956.

[66] G. Sharpe and S. Falle, "One-dimensional numerical simulations of idealized detonations," in *Proceedings of the Royal Society of London A: Mathematical, Physical and Engineering Sciences*, vol. 455, no. 1983. The Royal Society, 1999, pp. 1203–1214.

[67] K. Kailasanath, G. Patnaik, and C. Li, "Computational studies of pulse detonation engines-a status report," in *35th Joint Propulsion Conference and Exhibit*, 1999, p. 2634.

[68] P. Hwang, R. Fedkiw, B. Merriman, T. Aslam, A. Karagozian, and S. Osher, "Numerical resolution of pulsating detonation waves," *Combustion Theory and Modelling*, vol. 2, p. 1, 2000.

[69] C. K. Law, C. J. Sung, H. Wang, and T. Lu, "Development of comprehensive detailed and reduced reaction mechanisms for combustion modeling," *AIAA Journal*, vol. 41, no. 9, pp. 1629–1646, 2003.

[70] S. Yungster and K. Radhakrishnan, "Pulsating one-dimensional detonations in hydrogen–air mixtures," *Combustion Theory and Modelling*, vol. 8, no. 4, pp. 745–770, 2004.

[71] S. H. Kang, Y. J. Lee, S. S. Yang, M. K. Smart, and M. K. Suraweera, "Cowl and cavity effects on mixing and combustion in scramjet engines," *Journal of Propulsion and Power*, vol. 27, no. 6, pp. 1169–1177, 2011.

[72] H.-W. Yeom, B.-G. Seo, and H.-G. Sung, "Numerical analysis of a scramjet engine with intake sidewalls and cavity flameholder," *AIAA Journal*, vol. 51, no. 7, pp. 1566–1575, 2013.

[73] H. Ebrahimi, F. J. Malo-Molina, and D. V. Gaitonde, "Numerical simulation of injection strategies in a cavity-based supersonic combustor," *Journal of Propulsion and Power*, vol. 28, no. 5, pp. 991–999, 2012.

[74] B. J. Tatman, R. D. Rockwell, C. P. Goyne, J. C. McDaniel, and J. M. Donohue, "Experimental study of vitiation effects on flameholding in a cavity flameholder," *Journal of Propulsion and Power*, vol. 29, no. 2, pp. 417–423, 2013.

[75] K. Lee, S. Kang, Y. Lee, B. Cha, and B. Choi, "Effects of fuel injectors and cavity configurations on supersonic combustion," *Journal of Propulsion and Power*, vol. 29, no. 5, pp. 1052–1063, 2013.

[76] X. Cai, J. Liang, R. Deiterding, and Z. Lin, "Adaptive simulations of cavity-based detonation in supersonic hydrogen–oxygen mixture," *International Journal Of Hydrogen Energy*, vol. 41, no. 16, pp. 6917–6928, 2016.

[77] X. Cai, J. Liang, R. Deiterding, Z. Lin, and M. Sun, "Detonation interaction with cavity in supersonic combustible mixture," *AIAA Journal*, vol. 56, no. 5, pp. 2096–2102, 2017.

[78] S. A. Zhdan, "Mathematical model of continuous detonation in an annular combustor with a supersonic flow velocity," *Combustion, Explosion, and Shock Waves*, vol. 44, no. 6, pp. 690–697, 2008.

[79] J. E. Shepherd and P. Thibault, "Review of "the detonation phenomenon"," *AIAA Journal*, vol. 47, no. 5, pp. 1310–1311, 2009.

[80] C. M. Romick, "On the effect of diffusion on gaseous detonation," Ph.D. dissertation, University of Notre Dame, 2015.

[81] S. Singh, J. Powers, and S. Paolucci, "Detonation solutions from reactive Navier–Stokes equations," in *37th Aerospace Sciences Meeting and Exhibit*, 1999, p. 966.

[82] X. He and A. Karagozian, "Pulse-detonation-engine simulations with alternative geometries and reaction kinetics," *Journal of Propulsion and Power*, vol. 22, no. 4, pp. 852–861, 2006.

[83] ANSYS, "Ansys fluent theory guide, release 17.2," *ANSYS Inc.: Canonsburg, PA, USA*, 2016.

[84] G. J. Wilson and R. W. MacCormack, "Modeling supersonic combustion using a fully implicit numerical method," *AIAA Journal*, vol. 30, no. 4, pp. 1008–1015, 1992.

[85] S. Sato, A. Matsuo, T. Endo, and J. Kasahara, "Numerical studies on specific impulse of partially filled pulse detonation rocket engines," *Journal of Propulsion and Power*, vol. 22, no. 1, pp. 64–70, 2006.

[86] D. Anderson, J. C. Tannehill, and R. H. Pletcher, *Computational Fluid Mechanics and Heat Transfer*. CRC, 2016.

[87] D. C. Allgood, "An experimental and computational study of pulse detonation engines," Ph.D. dissertation, University of Cincinnati, 2004.

[88] Y. Wu, V. Yang, and S.-C. Chang, "Numerical simulation of detonation with detailed chemical kinetics using the space-time method," in *38th Aerospace Sciences Meeting and Exhibit*, 2000, p. 317.

[89] S. Gordon and B. J. McBride, "Computer program for calculation of complex chemical equilibrium compositions, rocket performance, incident and reflected shocks, and chapman–jouguet detonations," NASA SP-273, 2003.

[90] G. D. Smith, *Numerical Solution of Partial Differential Equations: Finite Difference Methods*. Oxford University, 1985.

[91] Y. Wada and M.-S. Liou, "An accurate and robust flux splitting scheme for shock and contact discontinuities," *SIAM Journal on Scientific Computing*, vol. 18, no. 3, pp. 633–657, 1997.

[92] J. Shepherd, "Chemical kinetics of hydrogen-air-diluent detonations.[Kinetic Models to Predict Detonation Cell Size]," Sandia National Labs., Albuquerque, NM (USA), Tech. Rep., 1985.

[93] G. Ben-Dor, *Shock Wave Reflection Phenomena*. Springer, 2007, vol. 2.

[94] H. D. Kim, S. J. Jung, T. Aoki, and T. Setoguchi, "A study of the weak shock wave propagating over a porous wall/cavity system," *Journal of Thermal Science*, vol. 14, no. 4, pp. 329–333, 2005.

[95] T. Endo, J. Kasahara, A. Matsuo, S. Sato, K. Inaba, and T. Fujiwara, "Pressure history at the thrust wall of a simplified pulse detonation engine," *AIAA Journal*, vol. 42, no. 9, pp. 1921–1930, 2004.

[96] L. Massa, J. M. Austin, and T. L. Jackson, "Triple-point shear layers in gaseous detonation waves," *Journal of Fluid Mechanics*, vol. 586, no. 205-248, pp. 512–526, 2007.

BIOGRAPHICAL STATEMENT

Sushma Yalavarthi was born in Vijayawada, India, in 1990. She received her B.S. degree in Aeronautical Engineering and Mathematics from the Aeronautical Society of India and Madras University, respectively, in 2013. She attended the University of Texas at Arlington (UTA) for her doctoral studies. She joined the Aerodynamics Research Center in 2016 as a Graduate Research Associate due to her interest in aerodynamics and gasdynamics. She was a recipient of the Tau Beta Pi student award. She has received several scholarships and served as a Graduate Teaching Assistant for various courses during her time at UTA. She is a student member of AIAA.